NUMERICAL AND EXPERIMENTAL STUDY OF IN-DRIFT HEAT AND MASS TRANSFER PROCESSES

Prepared for

U.S. Nuclear Regulatory Commission
Contract NRC–02–07–006

Prepared by

Kaushik Das[1]
Chandrika Manepally[1]
Randall Fedors[2]
Debashis Basu[1]

[1]Center for Nuclear Waste Regulatory Analyses
San Antonio, Texas

[2]U.S. Nuclear Regulatory Commission
Washington DC

September 2011

ABSTRACT

Water vapor flow and thermal environment near the emplaced waste can significantly affect the long-term repository performance. An interplay of chemical, thermal, hydrological, and geomechanical processes creates a complex environment that affects the water chemistry and water distribution pattern. Water source and distribution can affect the integrity of the engineered barrier system. Computational Fluid Dynamics (CFD) is an established numerical analysis method that has been used successfully to simulate ground water and vapor flow and thermal fields for a variety of applications. It provides an effective tool for quantitative analysis of the multiphase heat and mass transfer that takes place inside the drift. This report describes CFD tool development and validation activities that have been carried out at the Center for Nuclear Waste Regulatory Analyses. The general purpose CFD code ANSYS-FLUENT® Version 12.1 (ANSYS, Inc., 2009) was used to simulate the multimode heat and mass transfer within the drift. Modules were developed to simulate water evaporation and condensation, as the standard CFD solver does not have a suitable model to represent these processes. These modules were developed as customized functions and were linked with the main solver as User Defined Function. This report describes the development of the customized functions and in particular, assessment of these add-on functions to evaluate their suitability in simulating the in-drift heat and mass transfer processes. Two different experimental studies were conducted for benchmarking the simulated data. The first experiment was carried out in a closely controlled environment, where a single condensation-evaporation cycle was generated within a rectangular space. Temperatures at specific locations and condensation rates were measured. Subsequently, a model was developed using ANSYS-FLUENT to replicate the experimental setup and the customized functions were used to calculate condensation and evaporation rates. Computed results were compared with experimental data to gain confidence in the developed customized modules. The second experiment used for validation was a 20-percent drift-scale model of the repository using electrically heated cylinders to create the effect of heated waste packages and dripping water to replicate seepage. The experimental investigation studied both uniform and nonuniform heat load distribution and its effect on two-phase water movement within the drift. Numerical model results indicate the presence of strong vertical convection above the waste packages and within the gap between the cylindrical packages. Computed and experimental temperatures across the domain were compared and exhibited similar trends. Based on the benchmarking exercise, the developed modules were found to be suitable for their intended use for in-drift heat and mass transfer simulations.

Reference:

ANSYS, Inc. "ANSYS-FLUENT® Version 12.1 User's Guide." Canonsburg, Pennsylvania: ANSYS, Inc. 2009.

CONTENTS

Section Page

CONTENTS (continued)

Section Page

FIGURES

FIGURES (continued)

FIGURES (continued)

Figure Page

TABLES

ACKNOWLEDGMENTS

This report describes work performed by the Center for Nuclear Waste Regulatory Analyses (CNWRA®) and its contractors for the U.S. Nuclear Regulatory Commission (USNRC) under Contract No. NRC–02–07–006. The activities reported here were performed on behalf of the USNRC, Office of Nuclear Material Safety and Safeguards, Division of High-Level Waste Repository Safety. This report is an independent product of CNWRA and does not necessarily reflect the view or regulatory position of USNRC. The USNRC staff views expressed herein are preliminary and do not constitute a final judgment or determination of the matters addressed or of the acceptability of any licensing action that may be under consideration at USNRC.

The authors gratefully acknowledge T. Wilt for his technical review, E. Pearcy for his programmatic and editorial reviews, and B. Street for her administrative support. The authors would also like to acknowledge S. Svedeman, S. Green, and D. Bannon for their help in the design, fabrication, and performance of the test runs of the condensation cell. B. Bell and A. Walavalkar from ANSYS, Inc. are acknowledged for their advice and assistance in setting up the simulation cases and development of the User Defined Functions used in this study. M. Muller assisted with postprocessing results and developing graphics.

QUALITY OF DATA, ANALYSES, AND CODE DEVELOPMENT

DATA: All CNWRA-generated original data contained in this report meet quality assurance requirements described in the Geosciences and Engineering Division Quality Assurance Manual. Sources of other data should be consulted for determining the level of quality of those data. The work presented in this report is documented in Scientific Notebook No. 841E (Das, 2011).

ANALYSES AND CODES: The general purpose computational fluid dynamics simulation code ANSYS-FLUENT® Version 12.1 (ANSYS, Inc., 2009) was used to generate results for this report and is controlled in accordance with the CNWRA software quality assurance procedure Technical Operating Procedure–018, Development and Control of Scientific and Engineering Software. Postprocessing was done using TECPLOT 360 Version 2009 (TECPLOT, 2009).

References:

ANSYS, Inc. "ANSYS-FLUENT® Version 12.1 User's Guide." Canonsburg, Pennsylvania: ANSYS, Inc. 2009.

Das, K. "Unsaturated Zone Flow and Transport." Scientific Notebook No. 841E. San Antonio, Texas: CNWRA. 2011.

TECPLOT, Inc. "TECPLOT 360 Version 2009." Bellevue, Washington: TECPLOT, Inc. 2009.

1 INTRODUCTION

The in-drift repository environment is a result of a complex interaction between a number of thermal, hydrological and chemical processes. Numerical modeling techniques such as Computational Fluid Dynamics (CFD) that take into account the mutual interactions among these processes, can be useful to study such a multifaceted physical problem. The commercial off-the-shelf CFD package ANSYS-FLUENT® version 12.1 has been used for developing a baseline model for simulating the in-drift air flow and multimode heat transfer. In addition, customized User Defined Functions (UDFs) have been developed to include hydrological processes such as evaporation and condensation. This report summarizes the CFD model development, verification and benchmarking activities that have been carried out at the Center for Nuclear Waste Regulatory Analyses (CNWRA®). The verification and benchmarking calculation was supported by (i) a study of the condensation-evaporation cycle in a rectangular enclosure and (ii) a 20-percent drift-scale experiment of the proposed repository at Yucca Mountain. A brief description of these experiments is also provided in this report.

1.1 Background

This section presents a description of the in-drift physical processes that affect air flow and moisture movement. This section also provides a review of past experimental and modeling activities used in exploring the near-field in-drift thermohydrology.

1.1.1 Relevant Physical Processes

The water mass transfer and redistribution process within a drift is generally referred as cold-trap process. It is integrally linked with the thermally induced buoyancy driven natural convection of air within the drift as this is the primary mechanism of mass transfer. The cold-trap process is also fundamentally related to the interphase heat transfer processes at hot and cold surfaces, which act as the initial and terminal destination of water vapor within the system.

The proposed emplacement of high-level waste in drifts will significantly elevate the temperatures of the drift environment. Convection cells caused by temperature gradients along drifts will lead to the movement of air and water vapor. In the cold-trap process, water evaporates at hotter locations, is carried in the vapor phase by convective air flow, and condenses at cooler locations. Elevated relative humidity combined with deliquescence may lead to liquid phase water contacting waste packages initially in peripheral zones of the repository where the drift-wall temperature may not exceed the boiling point. As time proceeds and the thermal perturbation decays, this zone with potential deliquescence migrates inward toward the center of the repository. The geometry of the components of the engineered barrier system (e.g., waste package and support, drip shield, and invert) and interaction with the wallrock complicates the problem of simulating air flow and condensation associated with the cold-trap process.

Understanding convection in drifts is the first step for understanding the cold-trap process. Axial convection in the drift and latent-heat transfer will dampen axial temperature gradients. Offsetting this dampening is the heat flux from emplaced waste, which magnifies the temperature gradient between hot and cold locations. The intimate linkage of in-drift natural convection and condensation to heat and mass transfer in the host rock complicates modeling

efforts and requires the coupling of CFD and fluid flow in porous media models. The coupled simulations of porous media flow and in-drift flow using CFD codes will provide a detailed understanding of the involved physics. This coupling, however, is difficult because of the different time scales of the flow processes in the host rock and the drift. Porous media flow and heat transfer in the host rock has a much longer time scale, which ranges from months to years compared to the time scale of the convective flow in the drifts, which ranges from minutes to hours. Similarly, from Reynolds number (ratio of inertial to viscous forces in the flow space) considerations, independent CFD and porous media models are needed. Approximations of inertial flow effects at solid boundaries inherent in Darcy-based porous media models may not be valid for gas phase flow in large openings, such as the air spaces in drifts. These limitations have led researchers (Salari, 2005; Buscheck, et al., 2003) to develop independent models for the in-drift and surrounding porous host rock that are coupled through explicit exchange of boundary condition information between models at the interface. In general, separate CFD models are utilized for the large air spaces in drifts and porous media models for the fractured host rock. The question of explicit manual linkage or interactive dynamic linkage between these two approaches is a secondary issue at this point because of a larger question related to the sparseness of data to support any model results.

Conductive, radiative, convective, and latent-heat transfer processes all influence temperature estimates in the emplacement drifts. For all the solid objects present, including those of the engineered barrier system, conduction plays an important role. Radiation heat transfer is significant in the air space between the drift wall and engineered barriers. Natural air convection above and below the drip shield will lead to cross sectional and axial air flow that enhances heat dissipation from the heated waste packages. Individually, conduction, natural convection, thermal radiation, and interphase latent heat-transfer processes are reasonably well understood. The combined effect of all these modes of heat transfer in a geometrically complex underground environment, however, is still considered an area of active research. A number of challenges exist in the numerical modeling of such a system, such as the proper boundary condition at the porous host rock surface, accommodating a complex geometry, proper modeling of all the heat transfer processes, etc. As mentioned previously, the most well accepted method of determining the boundary condition is to use estimated temperature gradients using analytical heat transfer or thermohydrological porous media models to provide the boundary conditions to the CFD model (Buscheck, et al., 2003; Danko and Bahrami, 2004). A number of simplifications in the geometrical configuration, based on their relative importance on the heat transfer process, are done to develop a CFD model that can provide useful results while using reasonable computing resources. With the intent to retain the most relevant physics, approximations and assumptions are also used to simplify the conjugate heat transfer model, which may lack generality in terms of the range of application but provides valuable insight of the in-drift conditions in the proposed repository. This report describes the development of a model that is intended for simulating the in-drift environment. This report also presents discussion of the assumptions and approximations made during the model development process regarding boundary condition, geometry and pertinent heat transfer.

The general temperature and flow variation inside a drift are understood in terms of drift-scale {i.e., 1 km [0.6 mi]} and local-scale {i.e., <100 m [<328 ft]} variations. The local-scale variations are encountered in the immediate vicinity of a waste package and are generated mostly as a response to the magnitude of the thermal load of a single waste package or a series of neighboring waste packages. For example, local-scale variations are observed in the vertical natural convection pattern and the relative humidity around a waste package. Such local-scale convection cells can create a region of elevated or reduced temperature, reduced viscosity and

a preferential condensation zone within a drift. Drift-scale variations are broad patterns observed in the drift that are driven by the combined presence of a large number of waste packages within a drift. For example, the temperature difference between waste packages and drift wall will create a drift-scale convection that will tend to convect air in the axial direction. Similarly, heat load variation between two sets of waste packages that are placed far apart within a drift will start a convection current between the cooler and hotter region. It is clear that both local- and drift-scale variations contribute to the overall convection pattern and impacts moisture movement. A numerical model intended for resolving the in-drift flow and heat transfer processes should be capable of resolving both drift- and local-scale variations.

The cold-trap process involves transport of water vapor from a warmer to a cooler location. Available liquid water on a warmer surface will evaporate, and the evaporated water vapor will convect with air. The water vapor can condense to form liquid water in two different ways. If the moist air comes in contact with a relatively cooler surface, water vapor will condense on the cold surface, forming liquid water and will release the latent heat of condensation to the surface. This process is called surface condensation. On the other hand, if the convecting moist air enters into a relatively cooler fluid zone, water vapor will condense to form mist. In this case, the latent heat will be released to the surrounding air water vapor mixture. This process is termed volumetric condensation. This report provides details of the technical activities related to formulating, implementing and validating the evaporation condensation model that was used to supplement the baseline ANSYS-FLUENT solver.

1.1.2 Discussion on Previous Studies

A number of studies to understand the in-drift heat and mass transfered have been done by the U.S. Department of Energy (DOE) and the U.S. Nuclear Regulatory Commission (NRC). This section provides a very brief overview of these activities. A detail review of the literature is provided by Manepally, et al. (2006).

A comprehensive report by Bechtel SAIC Company, LLC (2004) described the DOE analysis pertaining to in-drift convection and condensation. DOE used two types of models to address in-drift convection and moisture redistribution: CFD and thermohydrological porous media models. CFD models focused on understanding in-drift processes and estimating the contribution of condensation to the flux of water entering the invert. Thermohydrological porous media models focused on incorporating the effect of in-drift processes on estimating temperature and relative humidity at the waste package and drip shield. To obtain the flow fields, DOE used the CFD code FLUENT®, which solves the time-averaged Navier-Stokes equations including turbulence and the energy equation including thermal radiation (Bechtel SAIC Company, LLC, 2004). Temperature variation along a drift in the surrounding host rock is included by incorporating 5 m [16 ft] of host rock (thermal model only) in the simulations. Two- and three-dimensional models are used to focus on issues at different scales, including representation of the drip shield, waste packages, and the invert in the grids. In the three-dimensional convection-only model, a 71-m [234-ft] portion of a drift (14 waste packages) is used as an analog for the much larger (~500-m [1640-ft]) emplacement half-drifts because of computational limitations. The two-dimensional representation uses the line-averaged waste package thermal loading and is used to gain confidence that radiation and turbulence in the gas-phase flow are accounted for in the three-dimensional model. A scaled down version of the repository illustrated the effect of including in-drift convection and moisture redistribution. A three-dimensional porous media model with three short drifts was simulated for three different

cases: (i) no axial transport in the drift or invert; (ii) a low value of a binary diffusion coefficient for axial transport, along with using pseudo-permeability and effective heat conductivity and adding a bulkhead; and (iii) a high value of a binary diffusion coefficient for axial transport, along with using pseudo-permeability and effective heat conductivity but no bulkhead (moisture and heat were allowed to escape to unheated portions of the drift). Bechtel SAIC Company, LLC (2004) concluded that the effect of convection and moisture redistribution on relative humidity, temperature, and rock saturation is encompassed in the broad range of uncertainty driven by percolation and host rock thermal conductivity.

The effect of natural ventilation through access tunnels and shafts in removing moisture from the drift and drift wall is well recognized . The concept is that moisture is removed from the emplacement drifts by exchange of air with the ground surface. The air at the ground surface generally has a low relative humidity at ground surface temperatures, and consequently an even lower relative humidity at emplacement drift temperatures. Danko and Bahrami (2006, 2003), however, have simulated the effects of natural ventilation by including the air pressure differences between drifts and the ground surface to approximate the air exchange in their model. Additional modeling using integrated in-drift and host rock models discussed in Birkholzer and Danko (2005), which may more realistically track moisture redistribution in the reflux zone during the thermal peak and continue after the wallrock temperatures have dropped below boiling, may be used to further study the effect of natural ventilation on moisture removal.

A number of independent studies performed at the CNWRA (Fedors, et al., 2004, 2003a,b) have evaluated the combined effect of in-drift natural convection with thermal radiation, conduction, and latent heat transfer using numerical (CFD) and laboratory models. These efforts have resulted in (i) development of increased understanding of the cold-trap process, (ii) identification of heat transfer processes to be explicitly represented in the CFD models, and (iii) experimental data not readily available in the literature that can be used to validate CFD models.

A prototype benchtop laboratory experiment was developed, details of which are given in Fedors, et al. (2003a) to provide measurement data for supporting models of air flow and moisture redistribution in nonventilated heated tunnels. The initial modeling effort did not match the experimental results with a high level of accuracy (Fedors, et al., 2003a). Two important processes lacking in early modeling efforts were identified: (i) the CFD simulations of the benchtop experiment did not explicitly track moisture movement, including phase change and latent-heat transfer and (ii) the simulations did not adequately track heat transfer at solid boundaries. The first reason identified for the poor match between the model and the experiment (the lack of a phase change model in the CFD code) was fixed by developing a Moisture Transport Module for FLOW-3D (Flow Science, Inc., 2005) that accounts for the mass transfer and latent heat transfer associated with the evaporation and condensation of water in the drift (Green, et al., 2004). CFD results obtained using the Moisture Transport Module better represent the expected relative humidity near the heat source. The low measured values of relative humidity near the heat source invalidate the previous assumption of 100 percent relative humidity used prior to implementation of the Moisture Transport Module. A second reason suggested for difficulties in matching measured temperatures near the heat source in the benchtop cold-trap experiment was the inadequacy of standard heat transfer models at interfaces of solids and air (Fedors, et al., 2003a). Later testing of heat transfer models simulated using detailed grids within the boundary layers at the solid-gas boundaries helped reduce uncertainty caused by heat transfer models (Fedors, et al., 2004).

Additionally, two other experiments were developed to provide measured data to support the parameters used in the CFD models. The first involved a small condensation cell intended to provide data for moisture redistribution using a geometry that allows tight control of conditions. Tests were conducted to measure (i) water evaporation and water condensation rates in a natural convection flow and (ii) the amount of water transported from the water source to the condensation plate. The measured water transport rates were used to validate the condensation-evaporation model developed for simulating the cold-trap process within ANSYS-FLUENT. Details of the experiment and the comparison of experimental and numerical data are presented in Chapter 3.

The second experiment used a 20-percent scale model of the emplacement drift with four analog waste packages providing a heat source in a long pipe. A detailed description of the 20-percent drift-scale experiment and the related CFD model is provided in Chapter 4 of this report. The valuable insights learned from the prototype benchtop experiment guided many of the design features of the 20-percent scale experiment. Green and Manepally (2006) had developed customized routines for simulating the moisture transport and thermal radiation models that were incorporated into a commercial CFD package FLOW-3D (Version 9.0). Details of this modeling exercise are reported in Manepally, et al (2006).

1.2 Organization of the Report

This report describes activities related to development, testing and benchmarking of a CFD modeling approach used to simulate in-drift heat and mass transfer including the cold-trap process. The commercially available CFD package ANSYS-FLUENT Version 12.1 is used as the platform for model development. Customized UDFs are developed to incorporate the condensation-evaporation modeling capability within the baseline ANSYS-FLUENT solver. Chapter 2 describes the mathematical basis along with approximations and assumptions for the condensation-evaporation modeling equations. A two-dimensional validation calculation is also described in Chapter 2. Flow of moist air over a cold plate and resulting condensation is simulated using the baseline ANSYS-FLUENT solver and customized UDFs. Results presented include general flowfield information and comparison of computed results with a closed form analytical solution. Chapter 3 describes a combined experimental and computational study to investigate the evaporation condensation process in a rectangular enclosure. The experiment measured temperature at specific locations in the domain along with condensation rate. The numerical model simulated the experimental setup in a two-dimensional domain. Results show the velocity, temperature and relative humidity distribution. A comparison of experimental and simulated data for condensation rate and temperature is also presented. Chapter 4 describes the laboratory and numerical model results of the intermediate scale experiment (20-percent drift scale). Experiments and computations were carried out for uniform and nonuniform thermal loadings. Numerical results are presented for temperature, relative humidity and velocity distribution in the flow field. A comparison of measured and computed temperature and relative humidity data are also made. The summary of this report is provided in Chapter 5.

2 NUMERICAL METHOD

Radioactive decay heat creates a natural circulation in the drift and heat dissipation takes place through conduction, convection and radiation. Additionally, the decay heat also initiates a condensation-evaporation cycle that involves latent heat exchange between phases. As mentioned in the previous chapter, simulation of in-drift thermal environment requires proper modeling of these coupled heat and mass transfer processes. Numerical models discussed in the report were developed using the general purpose commercial computational fluid dynamics (CFD) package ANSYS-FLUENT® Version 12.1 (ANSYS, Inc. 2009a,b). Though the baseline solver had adequate capabilities to model the heat transfer including radiation and mass transfer problem, development of customized functions was necessary to include the evaporation and condensation processes in the simulations. Capabilities of the baseline solver, technical basis for developing the customized functions, and their use are described in this chapter.

2.1 Description of the General Purpose Solver

ANSYS-FLUENT is a general purpose computational fluid dynamics (CFD) software package developed by ANSYS, Inc. It is widely used for design and analysis of applications ranging from aircraft components to sporting gear and garments. It is among the leading computer aided engineering tools that engineers use for flow, chemistry and heat transfer simulations in a continuum, though it also has some added modules for magnetohydrodynamics and discrete particle problems. To facilitate model development and pre and postprocessing activities, a number of additional software packages are also available. Three of these additional packages were used to build and analyze the models described in this report: (i) ANSYS-DesignModeler (ANSYS, Inc., 2009c), a computer aided design package for building geometries; (ii) ANSYS-Meshing (ANSYS, Inc., 2009d), used for mesh generation; and (iii) ANSYS-CFDPost (ANSYS, Inc., 2009e) for visualization and plotting.

ANSYS-FLUENT solves the generalized Navier-Stokes equations using the finite volume technique. It has a pressure- and a density-based solver to calculate the incompressible and compressible flows, respectively. The standard version of ANSYS-FLUENT has a comprehensive suite of models to represent conduction, convection, and radiation heat transfer with options to simulate phase change and solidification-melting phenomena. Radiation and phase change models were used extensively in the simulations described in this report. A number of multiphase flow modeling techniques including the volume of flow method, Eulerian-Eulerian model, mixture model, and the discrete particle tracking methods are available in the solver. The mixture multiphase model was used to account for phase dependent quantities in the numerical simulations reported here (ANSYS, Inc., 2009f).

The standard solver can be customized to meet the requirements unique to a particular application by using the user-defined functions (ANSYS, Inc., 2009g). Users can choose from a number of turbulence models ranging from zero equation models to large eddy simulation techniques available with the standard solver to simulate turbulence as their problems require. A number of spatial discretization schemes like the first-order upwind scheme, power law scheme, second-order upwind scheme, and central differencing scheme are available with both implicit and explicit time integration techniques for temporal terms of the equations. The simulation boundary conditions could be defined using the options available with the solver, or users can define it through customized functions. Most of the standard boundary conditions

such as the velocity and pressure inlet boundaries, outflows, periodic conditions, and solid wall conditions are available with the standard package. A large database of fluid and solid properties is also provided with the solver to model the presence of fluids, solids, and mixtures. Special boundary conditions and the modifications of equations needed for swirling and rotating flows and flows with nonstationary reference frames can be input as user options in the solver.

ANSYS-FLUENT uses an unstructured grid and supports a number of grid elements such as hexahedral, polyhedral, prismatic, and tetrahedral. A combination of hexahedral and tetrahedral meshes was used for building the models described in this report. The solver employs the Message Passing Interface routines for parallel processing on a number of platforms including Microsoft® Windows® NT, UNIX, and different variants of LINUX. The three-dimensional models described in Chapter 4 were solved using the parallel processing capability of ANSYS-FLUENT and were run on a LINUX cluster at the Center for Nuclear Waste Regulatory Analyses using 18 compute nodes.

2.2 Technical Requirements of Customized Functions

A set of customized functions was developed and plugged into the baseline solver to model the water-vapor –liquid phase change process. For the present application, three distinct possibilities were identified, where liquid-vapor phase change can take place.

1. Liquid water available at a relatively hot surface will evaporate from the surface and will use the hot surface as the source of latent heat.

2. Water vapor will condense to form liquid water in contact with a relatively cold surface and will use the cold surface as the sink of latent heat.

3. If the local temperature in certain areas drops below the saturation limit, moist air will partially condense to form liquid droplets. Condensation will continue until local equilibrium is achieved. In this situation, latent heat of condensation will be released to the surrounding air.

Assumptions were made to analytically quantify the mass and energy exchange as a result of these processes and to include them within the baseline simulation (discussed in the following section). The analytical formulation was subsequently coded as a User Defined Functions (UDFs) and was tagged with the main solver. The effects of these processes were incorporated as source terms of the governing equations and suitable boundary conditions.

2.2.1 Nomenclature

$\dot{m}'''_{H_2O}$	—	Volumetric mass source of water vapor in a computational cell (kg/m^3-s)
$\dot{m}'''_{air}$	—	Volumetric mass source of air in a computational cell (kg/m^3-s)
$\dot{m}'''$	—	Total (air + water) volumetric mass source (kg/m^3-s)
$\dot{m}''_{H_2O}$	—	Mass flux of water vapor through boundary layer (kg/m^2-s)
$\dot{m}''_{air}$	—	Mass flux of air vapor through boundary layer (kg/m^2-s)
$\dot{m}''$	—	Total (air + water) mass flux through boundary layer (kg/m^2-s)
n		Direction normal to the wall and assumed to be the y direction in the formulation
ρ	—	Mixture density (kg/m^3)

D	—	Diffusion coefficient (m^2/s)
y	—	Vertical distance from bottom wall (m)
v	—	Normal fluid velocity at the condensed water mixture interface (m/s)
ω_{H_2O}	—	Mass fraction of water vapor
$\omega_{H_2O}\ (T_{wall})$	—	Saturation mass fraction of water vapor at wall temperature $T_{wall}\omega_{air}$
	—	mass fraction of air
m_{cond}	—	Maximum condensable water vapor mass in volumetric condensation
$m_{f,cell}$	—	Cell water vapor mass fraction
$m_{f,saturated}$	—	Cell saturated mass fraction at cell temperature
f_{relax}	—	Relaxation factor for volumetric condensation
$\dot{m}$	—	Condensation rate due to volumetric condensation
S	—	Supersaturation Ratio
$(P_v)_{SSL}$	—	Vapor Pressure under supersaturation limit (Pa)
$P_{sat}(T)$	—	Saturation Vapor Pressure at Temperature T (Pa)
T	—	Cell Temperature (K)
J	—	Net flux of the number of droplet embryos {for droplet nucleation10^6 m^{-3}/s [2.831×10^4 ft^{-3}/s]}
σ	—	Surface tension between water droplets and surrounding moist air (N/m)
$\bar{M}$	—	Molecular Weight of moist air (kg/Kmol)
R	—	Universal Gas Constant (J/Kmol/K)
N_A	—	Avogadro Number [6.022141×10^{23}/mol]
K_B	—	Boltzmann Constant [1.38×10^{-23} J/K (5.657×10^{-24} ft-lb/^oR]
v_l	—	Specific volume of liquid water at cell temperature(m^3/kg)
$A_{cell\ wall}$	—	Face area of a computational cell at wall (m^2)
V_{cell}	—	Volume of a computational cell at wall (m^3)

2.2.2 Wall Condensation

The model for wall condensation was adopted from the study of Bell (2003) for condensation of superheated water on cold flat plate. It is conceptualized that condensation occurs as water vapor diffuses through the mass transfer boundary layer at the surface and on contact with the cold surface releases the latent heat to form a liquid film of water. The liquid film attains the wall temperature and the vapor diffusion and condensation continues at the liquid film-gas phase (air-vapor mixture) interface. This process is shown schematically in Figure 2-1. The rate of condensation is determined by the rate of vapor diffusion, which in turn depends on the difference in water vapor concentration across the boundary layer. On one end of the boundary layer is the bulk mixture and the concentration depends on the bulk flow parameters. The other end of the boundary layer is the condensed liquid water film and gas mixture interface. The present study assumes a local equilibrium at the liquid film-gaseous air water vapor mixture interface, which implies that the water vapor concentration at the interface is equal to the saturation value at the film temperature. Therefore, the film interface temperature dictates the concentration difference across the boundary layer and in turn controls the condensation rate.

The following assumptions are made regarding wall condensation in this analysis.

(i) Condensation occurs due to diffusion of water vapor through the species boundary layer. This assumption is used for deriving the mathematical expression for condensed water volume.

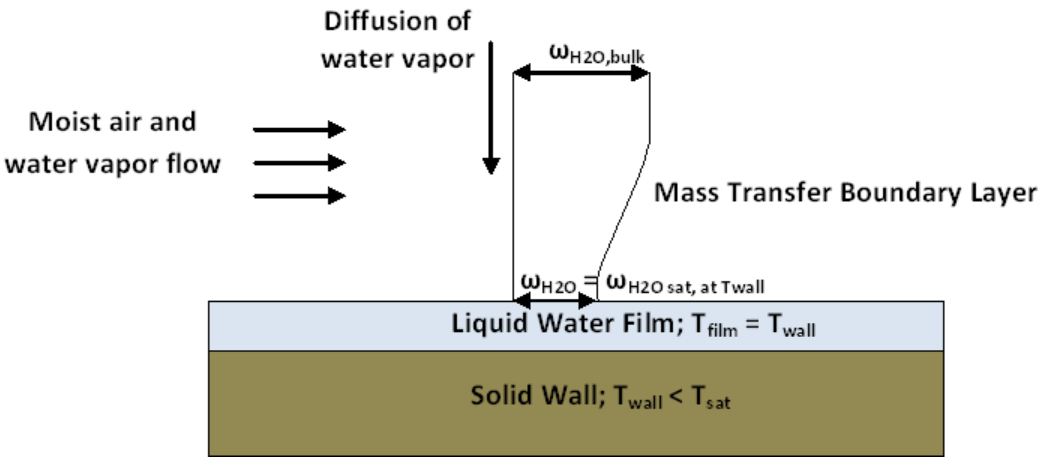

Figure 2-1. Schematic of the Condensation Model

(ii) The liquid film is in thermal equilibrium with the boundary wall and has the same temperature as the wall.

(iii) As discussed before, a saturation condition is also assumed at the liquid film-gas (air water-vapor mixture) interface. This implies that at the interface the partial pressure of water vapor is equal to the saturation vapor pressure at the cold wall temperature. This assumption, coupled with assumption (ii), indicates that the wall temperature dictates the water vapor concentration at the interface and in turn controls the total vapor diffusion and concentration rate across the boundary layer.

(iv) Any effect of the movement of liquid film is not considered. The liquid film may slide due to fluid shear and gravity, but it is assumed that the resulting motion does not affect the convecting airflow or subsequent condensation.

(v) Dropwise condensation is not considered and the analysis is restricted only to film condensation.

(vi) Any thermal resistance offered by the liquid film is not considered.

(vii) The liquid film consists of water and no other impurities exist.

(viii) Thermodynamic equilibrium is assumed at the liquid-film-air water-vapor mixture interface.

These assumptions are reasonable for the intended use of the developed UDFs, which is the condensation of water vapor within an underground drift. At the same time these assumptions also limit the use of the developed UDFs only for specific scenarios. Application of these UDFs to simulate a different environment will require a careful review of the effect of these assumptions on the problem to be modeled.

As mentioned previously, the condensation rate under these conditions is limited by the diffusion of water vapor towards the cold wall. The species mass flux equation for water vapor (Bird, et al.,1960; Bell, 2003) and air at the cold wall is written as

$$\dot{m}''_{H_2O} = -\rho D \frac{\partial \omega_{H_2O}}{\partial n} + \omega_{H_2O}\ \rho v \tag{2-1}$$

$$\dot{m}''_{air} = -\rho D \frac{\partial \omega_{air}}{\partial n} + \omega_{air}\ \rho v \tag{2-2}$$

From the definition of mass fraction we can conclude that

$$\omega_{air}\ = (1 - \omega_{H_2O}\ ) \tag{2-3}$$

$$\frac{\partial \omega_{H_2O}}{\partial n} = -\frac{\partial \omega_{air}}{\partial n} \tag{2-4}$$

The total mass flow through the boundary layer is given as

$$\dot{m}''\ = \dot{m}''_{air} + \dot{m}''_{H_2O} = \rho v \tag{2-5}$$

The air, however, does not dissolve into the liquid water film, and it is assumed that the mass flow rate of air is zero at the interface between liquid water and air-water vapor mixture. This assumption, along with Eqs. (2-1), (2-3), and (2-4), leads to the following relationship.

$$\rho v = \frac{1}{\left(\omega_{H_2O} - 1\right)} \rho D \frac{\partial \omega_{H_2O}}{\partial n} \tag{2-6}$$

From the mass continuity of a single computational cell near the boundary, the following relationship can be established

$$\dot{m}''' = \rho v \frac{A_{cell\ wall}}{V_{cell}} \tag{2-7}$$

The ρv term on the right hand side of Eq. (2-7) represents the flux that flows into a computational cell adjacent to a wall, and the product of the flux with the cell surface area at the cell-wall interface provides the total mass flow through the cell. It is assumed that the flow variables and properties do not vary considerably within a computational cell adjacent to the wall. This assumption is reasonable as long as the wall-adjacent cells are relatively small in size.

The total volumetric source term for the equation can be derived using Eqs. (2-6) and (2-7) as

$$\dot{m}''' = \frac{1}{\left(\omega_{H_2O} - 1\right)} \rho D \frac{\partial \omega_{H_2O}}{\partial n} \frac{A_{cell\ wall}}{V_{cell}} \tag{2-8}$$

The volumetric source term for water vapor in the cell can be calculated using Eq. (2-9)

$$\dot{m}'''_{H_2O} = \omega_{H_2O} \times \dot{m}''' \quad (2\text{-}9)$$

The mathematical expressions in Eqs. (2-1) through (2-9) were used in the baseline solver for calculating the source terms.

2.2.2.1 Source Term Specification

The baseline solver has the option of adding suitable source terms through customized user defined functions. The source terms for the governing equations are derived based on Eqs. (2-6) and (2-7) using the following method.

(i) The total volumetric source term obtained from Eq. (2-8) is used in the continuity equation.

(ii) The volumetric source term for water vapor obtained from Eq. (2-7) is used in the water-vapor species equation.

(iii) The momentum source terms for each direction were derived simply by taking the product of the total volumetric source term and the velocity in that direction.

(iv) The energy source term for the air-water vapor mixture was derived by taking the product of the total volumetric source term with the water vapor enthalpy value at the respective cell temperature. For wall condensation, the energy source term does not include any latent heat transfer term, because of the assumption that the liquid film and the boundary wall act as the sole energy sink for phase change. However, during volumetric condensation, the source term due to phase change is considered.

(v) For solid bodies present in the system, the energy source term is derived by taking the product of the volumetric source term for water vapor and the enthalpy of condensation. The total energy gain due to condensation of water vapor is applied to the solid body that contains the condensation surface.

These source terms were calculated through an UDF and were linked with the baseline solver.

2.2.2.2 Boundary Condition Specification

The other important aspect of modeling wall condensation is specification of the proper boundary condition. As per assumption (iii) in Section 2.2.2, a saturation condition exists at the interface between the liquid film and gaseous air-water vapor mixture. Thus, the relative humidity can be set to 100 percent and the water vapor pressure set equal to the saturation value at surface temperature. The corresponding mass fraction of the water vapor at the wall that contains liquid water will be the saturation mass fraction. The boundary condition at the wall is specified according to the equation below

$$\omega_{H_2O} = \omega_{H_2O,sat}(T_{wall}) \quad (2\text{-}10)$$

Eq. (2-10) accounts for the wall temperature effect on the condensation process. The wall temperature dictates the water vapor mass fraction specified at the wall and that in turn affects the vapor diffusion process described in Eq. (2-8). The saturation mass fraction of water vapor was determined from the ratio of saturation water vapor pressure and total cell pressure. The saturation water vapor pressure at cell temperature was determined using the functional relationship provided by Popiel and Wojtkowiak (1998).

The developed UDFs were used to specify the mass fraction profile as a function of the cell temperature. This UDF was linked as the water vapor species boundary condition at specific walls that have liquid water for evaporation or cold temperature conducive for condensation.

2.2.3 Wall Evaporation

The condensation model proposed by Bell (2003) was altered and adapted for evaporation. Evaporation took place from surfaces that had a film of water and had a temperature above the surroundings. Evaporation took place as the liquid water changed phase and diffused through the mass transfer boundary layer from the liquid layer to the air-water vapor mixture. The conceptual description of the evaporation process is described in Figure 2-2. Like the condensation rate, the evaporation rate is dependent on the rate of water vapor diffusion through the boundary layer. The diffusion rate of water vapor is proportional to the difference in water vapor concentration across the boundary layer. At the liquid-film-gaseous air water vapor mixture interface, an equilibrium condition is assumed, meaning that the concentration of water vapor at this interface is equal to the saturation concentration at the film temperature. Therefore, the film temperature dictates the rate of water vapor diffusion, which is assumed to be the evaporation rate.

The following assumptions are made regarding wall condensation in this analysis.

(i) Like condensation, evaporation is a multiphase process involving flow and coupled heat and mass transfer in both the liquid film and vapor. The physics can, however, be simplified as a scenario dominated by vapor diffusion through the species boundary layer. In this study, evaporation modeling assumes that evaporation is limited by the diffusion process through the species boundary layer. The mathematical expression for evaporated water vapor mass is derived based on this assumption.

(ii) The liquid film has the same temperature as the boundary wall.

(iii) The liquid water surface is saturated with vapor. Therefore, the partial pressure of water vapor is equal to the saturation vapor pressure at the liquid film temperature. This assumption, coupled with assumption (ii), establishes the influence of wall temperature on the evaporation rate.

(iv) A continuous water film is present on the surface where evaporation takes place.

(v) Motion of this liquid does not affect the evaporation process or the flow of the moist air water vapor mixture.

(vi) Thermal resistance of the liquid film is minimal and is not considered in the analysis.

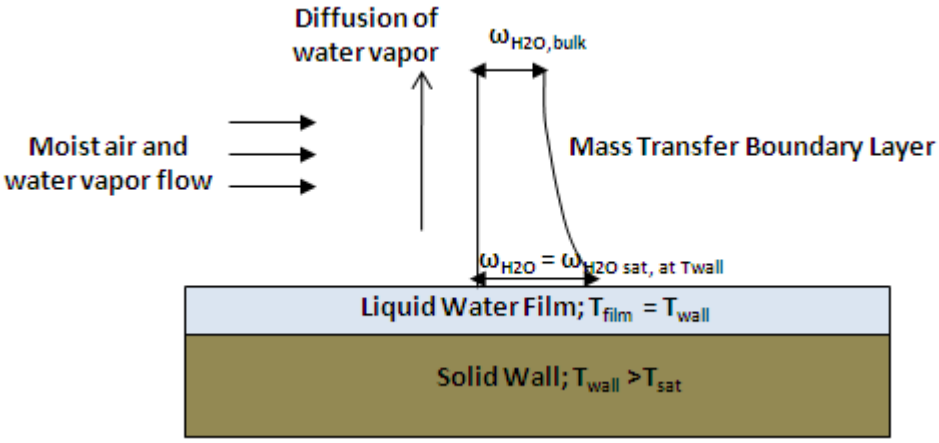

Figure 2-2. Schematic of the Evaporation Model

(vii) The liquid film consists of water and no other impurities exist.

(viii) Thermodynamic equilibrium is assumed at the liquid-film-air water-vapor mixture interface.

As the assumptions indicate, the basic heat and mass transfer processes in evaporation are similar to that of condensation. However, evaporation causes a net mass flow of water vapor from the surface to the flow through the mass transfer boundary layer. The basic process of mass transfer is diffusion controlled and the diffusion is driven by the concentration difference between the liquid water film and the main moist airflow. As a result, Eqs. (2-1) through (2-9) can be used to determine the volumetric source per computational cell generated due to evaporation, but the direction of mass flow needs adjustment. The system loses mass due to condensation and gains mass due to evaporation. To reflect this, the mass and water vapor species source terms derived in Eq. (2-8) will take the following form for evaporation modeling.

$$\dot{m}''' = \frac{-1}{\left(\omega_{H_2O} - 1\right)} \rho D \frac{\partial \omega_{H_2O}}{\partial n} \frac{A_{cell\ wall}}{V_{cell}} \tag{2-11}$$

Equation 2-11 is used to derive source terms for the governing equations for the evaporation process. The method of calculating the source terms for governing equations from the volumetric mass source term is described in section 2.2.2.1. The boundary condition for evaporation was specified using a mass fraction profile was derived based on the saturation condition at the wall temperature. As it is assumed that a saturation condition exists at the liquid film surface, the relative humidity is fixed at 100 percent. The relative humidity value was used to determine the mass fraction of water vapor. Equation (2-12) was used to specify the species boundary condition at the wall where evaporation is expected to take place.

$$\omega_{H_2O} = \omega_{H_2O,sat}\left(T_{wall}\right) \tag{2-12}$$

The baseline ANSYS-FLUENT solver does not have the option to specify the required species boundary condition. Therefore, a UDF was developed based on Eq. (2-12) to implement the boundary condition and was linked with the baseline solver.

2.2.4 Volumetric Condensation

Volumetric condensation takes place if convecting moist air encounters a local temperature that is below the saturation temperature. As the fluid temperature drops, relative humidity increases gradually and reaches 100 percent at the saturation temperature. A further drop in temperature will result in condensate formation. A number of assumptions are made with regard to volumetric condensation modeling.

(i) Condensed liquid water forms a mist and is convected with the moist air as a separate phase.

(ii) Volumetric condensation formation is assumed to take place only due to droplet nucleation; bubble nucleation is not considered in the analysis.

(iii) Coalescence, breakup or subsequent evaporation of the liquid droplets is not considered.

(iv) Wall interaction with the liquid droplets is not taken into account. This implies the liquid droplets behave the same way as moist air when it comes in contact with a wall.

(v) A mixture model is used to solve the governing equations for the two-phase 'moist' air-liquid droplet flows. Specifically, the model solves the momentum, continuity, and energy equations for the mixture, the volume fraction equations for the secondary phases, and algebraic expressions for the relative velocities.

Based on these assumptions, two different approaches were adopted for modeling the volumetric condensation process and are described in the next section. These two approaches are called equilibrium and nonequilibrium models, based on their treatment of the thermodynamic condition in a computational cell. The equilibrium approach was used by Hijikata and Mori (1973) and Brouwers and Chester (1992a,b) whose formulation depended on boundary layer analysis. Later Fox, et al. (1997) adopted this approach to study condensation and mist formation in closed enclosures. Fox, et al. (1997) also formulated a nonequilibrium model and a modified critical saturation model and showed that the experimental data lie somewhere between the equilibrium and nonequilibrium predictions. Kang and Kim (1999) used both equilibrium and nonequilibrium methods to characterize film condensation of a supersaturated steam-air mixture on a flat plate. They found the model performance was dependent on the temperature difference between the supersaturated hot gas and cold condensation plate. At a low temperature difference, the computed results matched experimental observations, with no mist generation. On the other hand, at a high temperature difference, the nonequilibrium model performed better.

2.2.4.1 Equilibrium Model

In this approach, it is assumed that the condensation process will continue until local thermodynamic equilibrium is reached. This implies that supersaturation of the mixture is not

allowed and any water vapor that is in excess of the saturation limit will condense. Based on this understanding, the total mass available for condensation in a single computational cell can be expressed as

$$m_{cond} = \rho(m_{f,cell} - m_{f,saturated}) \tag{2-13}$$

Where $m_{f,saturated}$ can be determined based on the ratio of cell saturation vapor pressure and cell total pressure. The cell saturation vapor pressure was determined using the functional relationship provided by Popiel and Wojtkowiak (1998). All of the simulations described for the current report assume a steady state behavior, and all the water vapor available for condensation will change phase to form liquid as the solver converges to a steady solution. Numerical stability considerations, however, limit the quantity of mass that can be condensed in a single iteration as the solution progresses. As a result, a relaxation factor was introduced to achieve numerical stability. The modified equation provides a condensation rate estimate

$$\dot{m} = f_{relax} \times \rho(m_{f,cell} - m_{f,saturated}) \tag{2-14}$$

The relaxation factor f_{relax} was determined using numerical experiments as it depends on the local thermodynamic condition, moisture content and other numerical and modeling parameters. It was found that the value of this factor can range between 0.3–0.9. The factor is allowed to have high values for a system with lower level of supersaturation.

2.2.4.2 Nonequilibrium Model

The nonequilibium model assumes that a level of supersaturation will exist in fluid. In this case, not all of the available water vapor mass that is in excess of the saturation limit will condense. The limit of supersaturation is determined using kinetic theory and is given by the following equation (Carey, 2007)

$$S = \frac{(P_v)_{SSL}}{P_{sat}(T)} = \exp\left[\frac{E^*(-\ln J^{*1/2})}{2(E^*)^{1/2} + (-\ln J^{*3/2})}\right]^{1/2} \tag{2-15}$$

Expressions of E^* and J^* are provided in the following equations

$$J^* = \frac{\bar{M}J}{N_A v_l}\left(\frac{tt\bar{M}}{2\sigma N_A}\right)^{1/2}\left[\frac{RT}{P_{sat}(T)}\right] \tag{2-16}$$

$$E^* = \frac{16\pi\sigma^3 v_l^2}{3k_B R^2 T^3} \tag{2-17}$$

The condensation rate calculated using the nonequilibium model is given by the following relation.

$$\dot{m} = f_{relax} \times \rho(m_{f,cell} - S \times m_{f,saturated}) \tag{2-18}$$

Hence the vapor mass available for condensation is reduced by the supersaturation limit S.

2.2.4.3 Source-Term Calculation

A UDF was developed to calculate the mass transfer rate from the vapor to liquid phase as described in Eqs. (2-14) and (2-18) (Carey, 2007; Fox et al. 1997). Based on these quantities, the source terms were calculated for species, mass, momentum and energy equations. For the species and mass conservation equation, the source is obtained directly from Eqs. (2-14) and (2-18). The source terms for the momentum equations are obtained by taking the product of mass source term with velocity. The energy equation source term was determined by taking the product of the mass source and latent heat of condensation. The latent heat of condensation for the system pressure was obtained from a functional relationship provided by Popiel and Wojtkowiak (1998).

2.3 General Numerics

This section describes the numerical parameters that were used in all the simulations described in this report. A variety of spatial and temporal discretization schemes as well as turbulence models are also available in ANSYS-FLUENT. Simulation parameters were chosen as suitable for natural convection flows. For the present simulations, the pressure-based solver was chosen, as the flow can be considered to be in the incompressible fluid. The two-dimensional Navier Stokes equations were solved using an implicit approach. The Semi-Implicit Pressure Linked Equations–Consistent (SIMPLEC) algorithm (Van Doormal and Raithby, 1984) was used to treat pressure velocity coupling for numerical stability. The third order Monotone Upstream-Centered Schemes for Conservation Laws (MUSCL) were used to derive the surface values of different variables for the spatial discretization, used to compute the convective fluxes. The Rhie-Chow scheme (Rhie and Chow, 1983) was selected to interpolate pressure at the control volume face and to satisfy mass conservation without pressure oscillations. Wherever applicable, the shear stress transport k-ω model (Menter, 1994) was used to simulate turbulence.

A number of radiation models are available in the baseline CFD solver, including the surface-to-surface, Rosseland, Discrete Transfer of Ray and this discrete ordinate model. Based on previous studies (Das, et al, 2007, 2008) and guidelines provided by ANSYS-Fluent (ANSYS, Inc., 2009a) for modeling radiation in a nonparticipating media with natural convection, the discrete ordinate model was chosen for the present study. In this approach, the radiative transfer equation for an absorbing, emitting, and scattering medium is solved for a finite number of discrete solid angles. In the current study, four angular discretizations were used in each direction of the spherical coordinates system.

2.4 Verification Calculation

A simulation was carried out to verify the accuracy of the developed UDFs. The simulation was adopted from the study of Bell (2003). The study of Bell (2003) simulated flow of supersaturated water vapor over a cold flat plate and wall film condensation. The numerical study presented in the current report considers volumetric condensation in addition to wall film condensation.

The computational domain, grid, and boundary conditions for the condensation problem are shown Figure 2-3. Moist air flows inside the domain at inlet. The lower wall is maintained at a

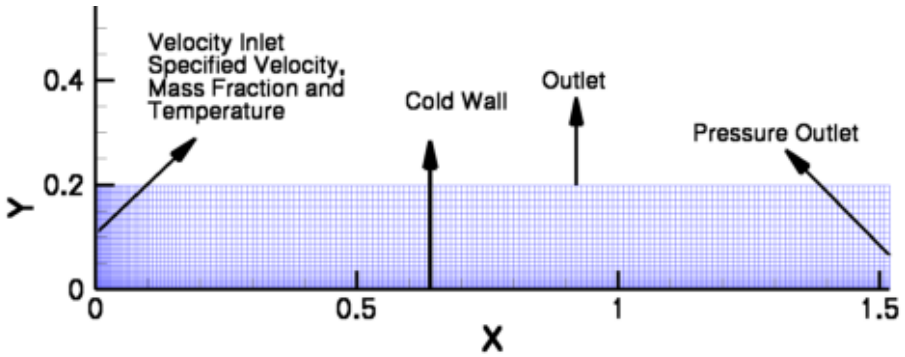

Figure 2-3. Schematic for Condensation of Humid Air Over Flat Plate

lower temperature compared to the moist airflow. As a result, condensation takes place at the cold wall. Sparrow, et al. (1967) derived an analytical solution for this problem.

2.4.1 Description of the Numerical Model

The test case is modeled as a two-dimensional steady laminar two-phase flow problem, and the incompressible Navier-Stokes equations are solved without using any turbulence models. Species transport equations with inlet diffusion and diffusion energy source are solved for the vapor phase. Two different velocities with a fixed water vapor concentration at the inlet are studied, and results are compared with experimental data. The fluid in the domain is specified as a mixture of water vapor and air, and the density of the fluid is determined using the volume-weighted mixing law. The customized UDF to incorporate the source terms is compiled and linked with the mass, momentum, energy, and species transport equations using the standard ANSYS-FLUENT interface.

A mixture of water vapor and air is specified as the working fluid in the domain. The free stream velocity is specified at the velocity inlet of the domain along with temperature and mass fraction of water vapor. A pressure outlet boundary condition with specified backflow temperature and water vapor mass fraction is specified at the downstream outlet as well as at the top of the domain. A number of customized source terms for the continuity, momentum, energy, and species equations are introduced through UDFs to model the effect of mass removal due to condensation at the cold bottom wall. To capture the boundary layer and the condensation process, grids are clustered near the bottom wall.

Both equilibrium and nonequilibrium models were used separately for the problem. Figures 2-4 through 2-7 show results obtained using the nonequilibrium model, whereas Figures 2-8 through 2-11 highlight results obtained from the equilibrium model that accounts for interphase mass transfer due to volumetric condensation. Both these test cases were run for two different mixture inlet velocities of 1 m/s [3.28 ft/s] and 0.1 m/s [0.33 ft/s] but the mass fraction of vapor in the mixture was fixed at 0.47967.

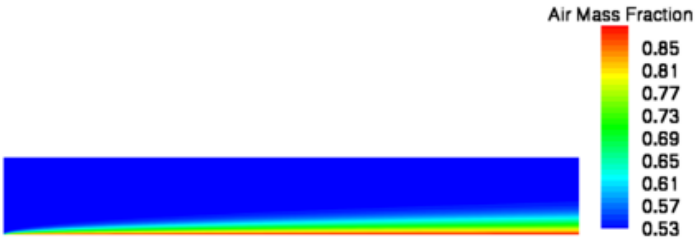

Figure 2-4. Air Mass Fraction Variation in the Flow Field

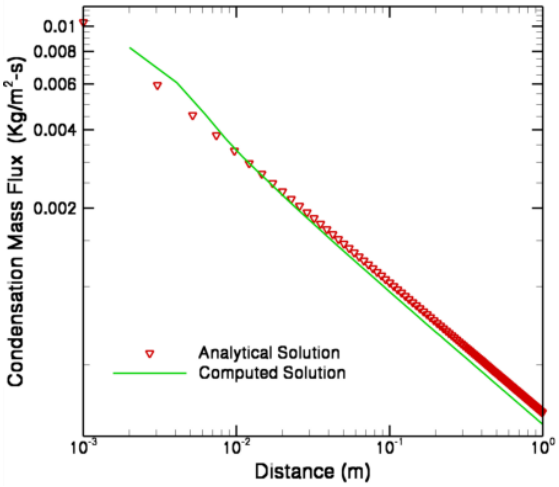

Figure 2-5. Comparison of Analytical and Computed Results for Condensation Mass Flux for Inlet Velocity = 0.1 m/s [0.33 ft/s] Using Nonequilibium Model [1 m=3.28 ft; 1 kg/m^2-s =0.205 lb/ft^2-s]

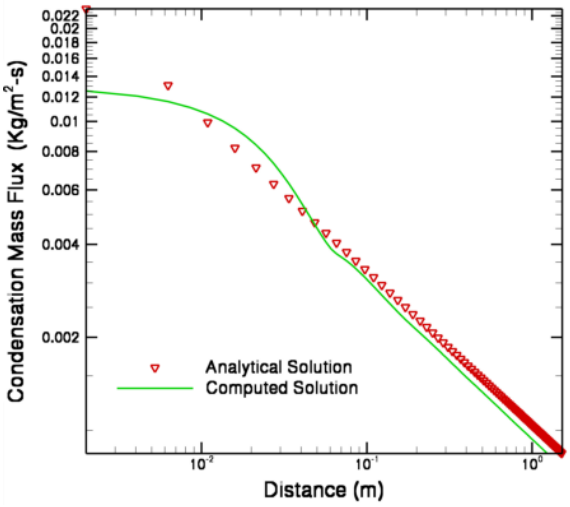

Figure 2-6. Comparison of Analytical and Computed Results for Condensation Mass Flux for Inlet Velocity = 1 m/s [3.28 ft/s] Using Nonequilibium Model [1 m=3.28 ft; 1 kg/m^2-s =0.205 lb/ft^2-s]

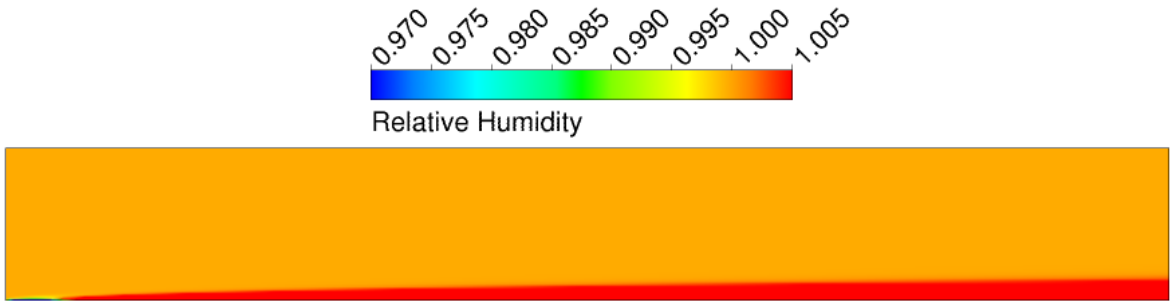

Figure 2-7. Relative Humidity Contours for Simulation Using Nonequilibium Model and Inlet Velocity = 1 m/s [3.28 ft/s]

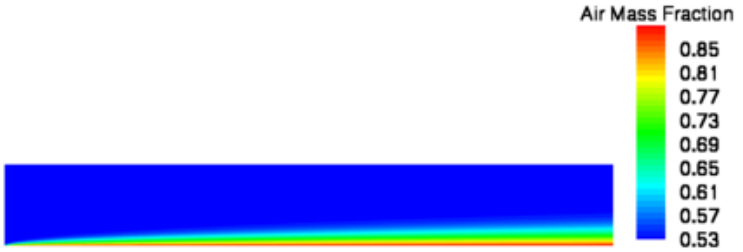

Figure 2-8. Air Mass Fraction Variation in the Flow Field With Multiphase Flow and Inlet Velocity = 1m/s [3.28 ft/s]

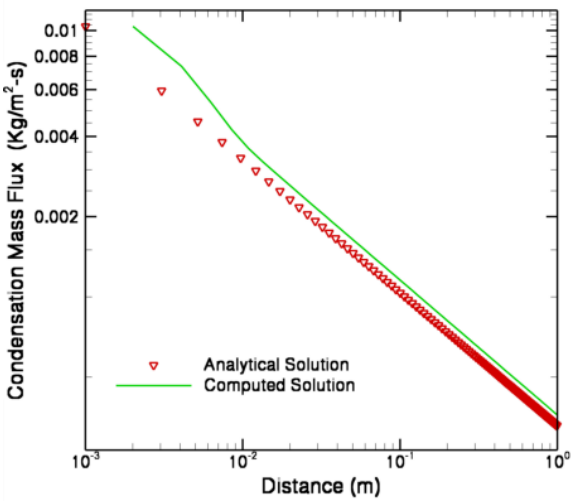

Figure 2-9. Comparison of Analytical and Computed Results for Condensation Mass Flux for Inlet Velocity = 0.1 m/s [0.33 ft/s] Using Equilibrium Model [1 m=3.28 ft; 1 kg/m^2-s =0.205 lb/ft^2-s]

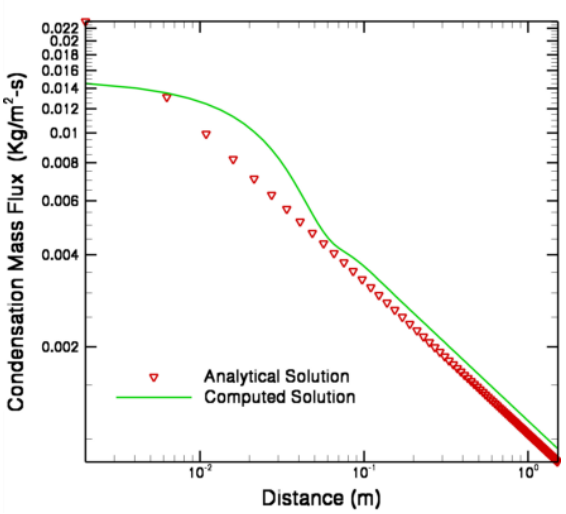

Figure 2-10. Comparison of Analytical and Computed Results for Condensation Mass Flux for Inlet Velocity = 1 m/s [3.28 ft/s] Using Equilibrium Model [1 m=3.28 ft; 1 kg/m^2-s =0.205 lb/ft^2-s]

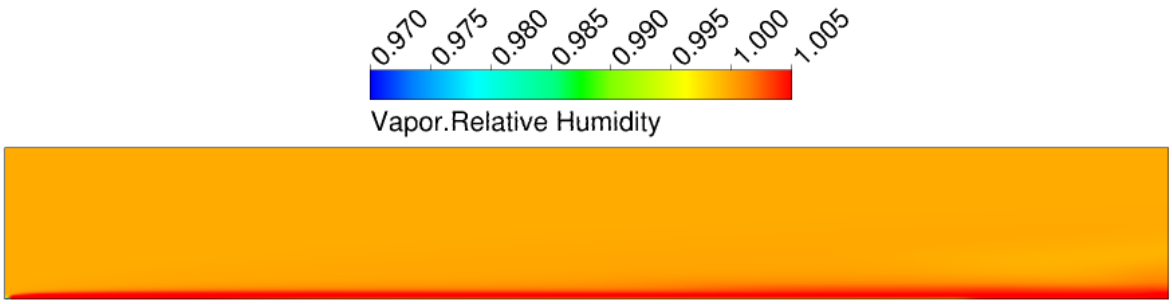

Figure 2-11. Relative Humidity Contours for Simulation With Multiphase Species Transport and Inlet Velocity = 1 m/s [3.28 ft/s]

2.4.2 Test Results for Nonequilibrium Model

The air mass fraction contours for an inlet velocity of 1 m/s [3.28 ft/s] are shown in Figure 2-4. The thickness of the air mass fraction increases along the cold wall because the mixture loses water vapor due to condensation and the mass fraction of water vapor in the mixture decreases. Consequently, the mass fraction of air in the mixture increases near the bottom wall of the domain. This is consistent with the understanding of the physics of film condensation on cold flat plates.

Figure 2-5 compares condensed mass flux at the cold bottom wall for an inlet velocity of 0.1 m/s [0.33 ft/s]. In the downstream region, the pattern of the computed results is in good agreement with the analytical solution, though the computed result slightly under predicts the data.

The analytical and computed solutions have some deviation near the leading edge of the plate {0–0.1 m [0–0.328 ft]}, though near the trailing edge {0.8-1 m [2.62–3.25 ft]} the deviations do not exceed 10 percent of the overall range. The computed solutions do not take into account the boundary layer development and assume a fully developed boundary layer from the leading edge. Thus, the leading edge results should be excluded from the comparison and the study is considered validated only for the downstream flow. The deviation in the trailing edge occurs because the analytical solution makes certain assumptions regarding the boundary layer thickness near the plate leading edge that are different from the simulated case.

Figure 2-6 compares the computed and analytical solution for an inlet velocity of 1 m/s [3.28 ft/s] and shows the same trend as in the previous test case with a different inlet velocity. The results show some deviation between simulated and analytical solution is within 10 percent based on the total range.

Figure 2-7 shows the contours of relative humidity of the entire flow domain for an inlet velocity of 1 m/s [3.28 ft/s]. The results show that though the majority of the domain is either at a saturated or unsaturated condition, there is a thick layer near the condensation zone that shows supersaturation. As mentioned in Section 2.2.4.2, the nonequilibrium solution does not consider complete volumetric condensation where the excess water vapor that causes supersaturation is partially allowed to remain in vapor phase. As a result, a small section of fluid near the boundary layer is supersaturated.

2.4.3 Test Results for Equilibrium Model

Figure 2-8 shows calculated concentration of air in the domain using equilibrium model. The result is similar to the concentration distribution obtained using nonequilibrium model. This similarity is due to the lack of volumetric coordination in the main flow away from the wall. As there is negligible volumetric condensation, equilibirum and nonequilibrium models work the same way and calculates similar concentration distribution. Due to a high wall condensation rate, the air mass fraction near the bottom cold wall is affected. Inside the domain, away from the wall, volumetric condensation is the only mechanism that can affect species distribution. Because the volumetric condensation rate is orders of magnitude less than the wall condensation rate, the species distribution appears to be unaffected.

Figures 2-9 and 2-10 show the wall condensation mass flux for two different equilibrium model test runs. In general, both the runs reasonably predict the experimental data.

However, unlike the test cases described in Section 2.4.2 in connection with the nonequilibrium model where the computed results slightly under-predicted the condensation rate, here the computed solution slightly over-predicts it. The disparity between the computed and the analytical solution in the upstream region is higher compared to the nonequilibrium model solution. This can be attributed to a number of factors.

1. The analytical solution was derived for wall condensation only and did not consider volumetric condensation. Thus, some disagreement between the equilibrium model solution, which considers volumetric condensation, with analytical solution was expected.

2. Removal of water vapor from the mixture phase may have caused a steeper gradient of species concentration, causing a higher diffusion flux of water vapor towards the wall.

3. The volumetric condensation process affects the species distribution of water vapor near the cold wall and can affect the diffusion flux of water vapor through the boundary layer that ultimately affects the condensation rate.

4. A number of assumptions regarding boundary layer development were made in the analytical solution near the flat plate leading edge which are not present in the computational solution. The boundary layer development in the computational solution did not follow the prescribed profile specified for the analytical solution.

Figure 2-11 shows the relative humidity contours for the flow domain. The results show that the relative humidity pattern obtained using the equilibrium model are different from that obtained using the nonequilibium model. In the results obtained using equilibrium model, the supersaturation layer has been reduced significantly. Ideally, the entire domain should either be at an unsaturated or saturated condition. The nonequilibium model was not able to completely remove the extra water vapor responsible for saturation due to stability issues with the numerical solution. This problem is encountered for systems with a higher level of moisture content and will not pose a problem for systems with moderate or low levels of moisture content.

The verification calculation in this chapter shows that the UDFs for volumetric and surface condensation were able to calculate a flow field that matched experimental data with less than 10 percent deviation. The nonequilibrium model produced relatively better results than the analytical solution which did not consider volumetric condensation. The relative humidity calculated using the equilibrium model was, however, more realistic as supersaturation was not allowed.

2.5 Summary

This chapter discusses the numerical approach utilized to study the condensation-evaporation cycle along with natural condensation in the cold-trap process. ANSYS-FLUENT Version 12.1 is used as the general baseline solver for the problem. A set of customized UDFs were developed to model the condensation and evaporation processes. The mathematical bases for the wall evaporation and condensation models were discussed. The volumetric evaporation process was modeled using two different approaches depending on the treatment of thermodynamic equilibrium of the system. The equilibrium model assumed that the volumetric condensation process will continue until a saturation condition is attained. On the other hand, the nonequilibrium model allowed partial supersaturation and the level of supersaturation was obtained using kinetic theory. A verification calculation was done where an analytical solution for the condensation rate of hot moist air on a cold plate was compared with simulated data. This study provides confidence in the analytical formulation of the condensation and evaporation processes and the implementation of these mathematical expressions as UDFs.

3 CONDENSATION CELL EXPERIMENT AND VALIDATION

Two detailed laboratory tests were conducted to verify the overall modeling capabilities of the ANSYS-FLUENT® solver in predicting the flow and thermal field. The first set of experiments used a small-scale laboratory model to validate the user defined modules for calculating the wall and volumetric evaporation-condensation process. The environment within the test chamber was well controlled and regulated. The experiments were conducted to obtain measurements of water transport rates in a simple two-dimensional natural convection flow. To simplify the validation experiments, low temperatures and temperature gradients were used so that radiation could be neglected. The intent of these experiments was to make a quantitative comparison between the experimentally obtained and computed condensation rates and air temperatures. This chapter will first describe the small-scale experiments and their results for temperature distributions and condensation rates. Subsequently, development of the corresponding numerical model will be described and results from the computational fluid dynamics (CFD) analysis will be compared to the measured water transport rates.

3.1 Description of Water Transport Experiments

Laboratory tests were conducted to measure the amount of water transported from a heated water source to a cold (condensation) plate. Multiple tests were conducted by varying the heat rate to the water source and varying the temperature of the cold plate. Once steady state temperatures were attained, water transport rates were determined by collecting condensation draining from the cold plate. A description of the test chamber is given below.

3.1.1 Test Chamber

A schematic diagram and photographs of the test chamber are shown in Figures 3-1 and 3-2, respectively. The enclosure was made of polycarbonate sheet, acrylic sheet, and aluminum. Water evaporates from the heated tray shown on the bottom left of the enclosure. Water was continuously added to the water tray to maintain the level. Water was condensed and collected on the cooled aluminum plate shown on the right side of the test enclosure. Instrumentation was included to measure the evaporator (water) temperature, condenser temperature, air temperatures, and the water condensation rate.

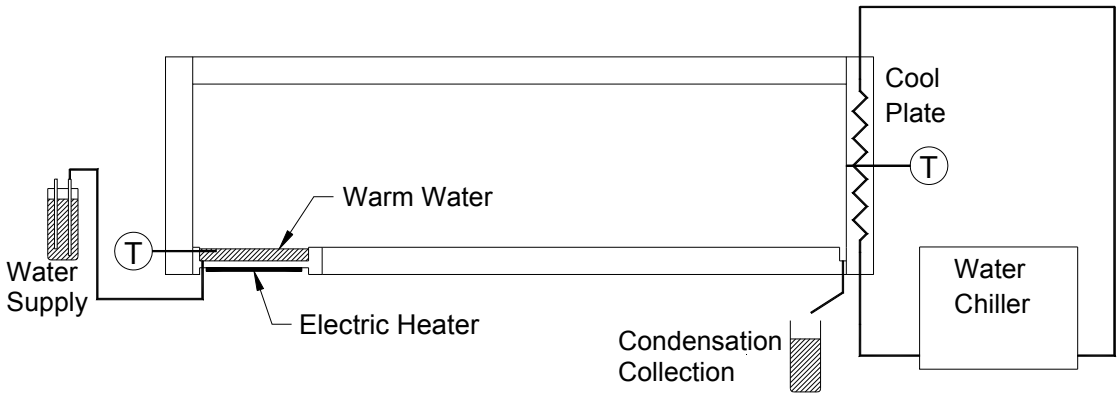

Figure 3-1. Side View Schematic of Laboratory Test Chamber

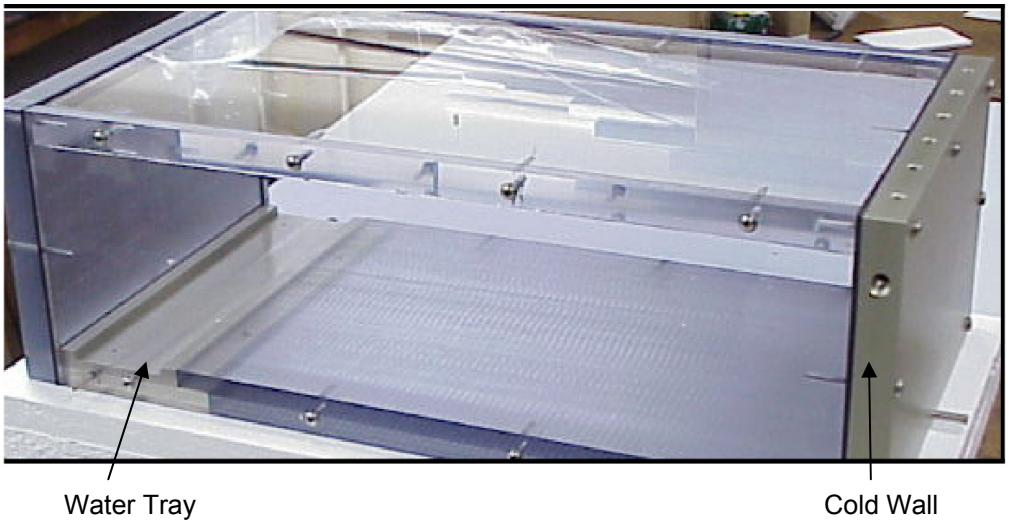

Figure 3-2. Side View Photographaboratory Test Chamber

The chamber was 0.584 m [23 in] long, 0.154 m [6 in] tall and 0.305 m [12 in] deep. The tray holding the source water was 0.076 m [3 in] long and ran the entire 0.584 m [12 in] depth of the chamber. The top wall of the chamber was made from 0.025 m [1 in] thick acrylic. The left end wall and bottom wall were made of 0.025 m [1 in] thick polycarbonate. The water tray placed at one end of the bottom wall, as shown in Figure 3-2, was made of aluminum. The front and back walls of the chamber were made of 0.013 m [0.5 in] thick polycarbonate. The cold plate was made of 0.025 m [1 in] thick aluminum and had channels drilled through it to allow the circulation of cooling fluid through the plate. Though not shown in Figure 3-2, the entire chamber was covered with a 0.025 m [1 in], and later 0.050 m [2 in], thick shell of polystyrene foam insulation to reduce heat transfer between the experimental chamber and the surroundings. The chamber was placed on top of a table and to reduce heat transfer, two sheets of polystyrene foam insulation were placed between the chamber and the table top.

External thermal energy was provided for warming the water using an electric heater, which was attached directly to the bottom of the aluminum water tray. The heater pad had the same dimensions as the water tray, which was 0.076 m [3 in] long by 0.305 m [12 in] deep. The power to the heater pad was supplied by a variable power source. The goal of the heating and cooling component design in the chamber was to create a two-dimensional convection cell in the plane along the length and height of the chamber, with minimal variation in the third direction. Temperature measurements were made at the centerline of the 0.305 m [12-in] depth of the rectangular domain.

Thermocouples were installed in the test chamber to measure the temperature and their locations are shown in Figure 3-3. The thermocouples were Omega, Type K, model number 5TC TT K 30 72 with a bare wire junction and 25 $\times 10^{-5}$ m [0.01 in] diameter wire. A calibration check showed that all of the thermocouples were within 0.2 $^{\circ}$C [0.36 °F] of the standard thermometer reading.

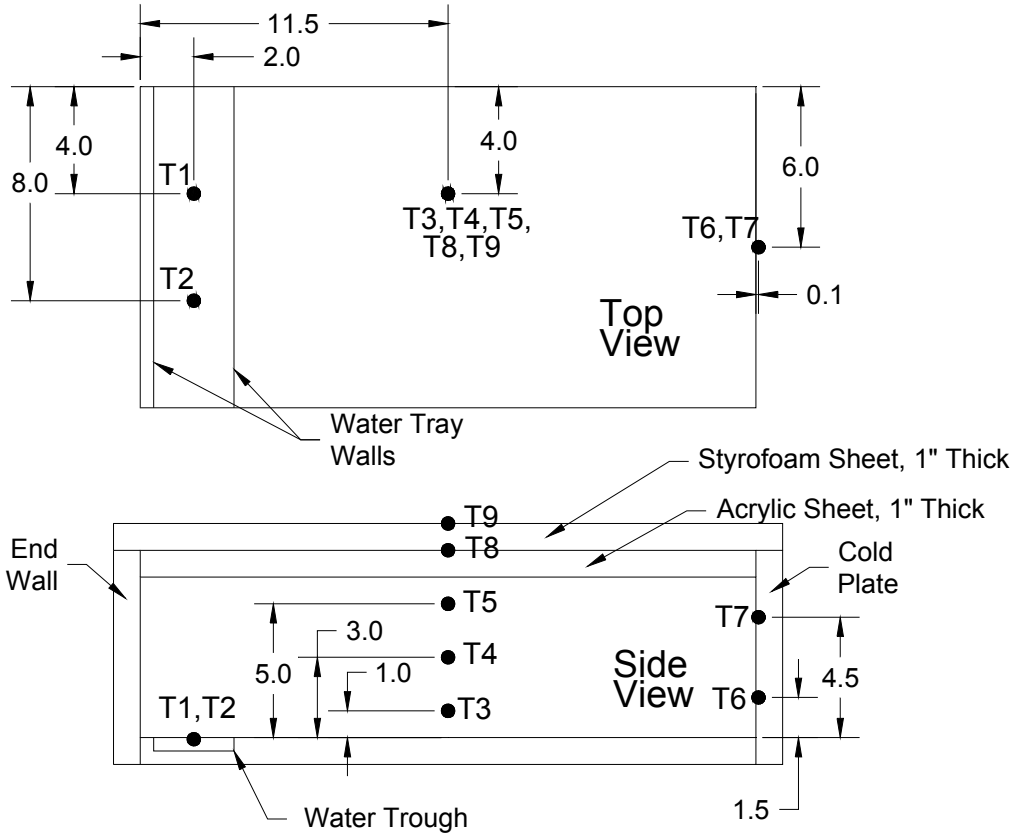

Figure 3-3. Top and Side Views Schematic of Laboratory Test Chamber. All Dimensions Are in Inches. T1 to T9 Are Thermocouples. [1 m = 39.37 in]

Water that condensed on the cold plate was drained off and collected in a graduated cylinder to measure the condensation rate. Depending upon the condensation rate and collection time, different size graduated cylinders were used to collect the fluid to improve measurement resolution. Several tests were initially performed without water to test the estimation of convection velocities and temperatures in a simpler regime and prepare the system for actual tests. Results of these initial runs are not discussed in this report.

3.1.2 Observations and Test Measurements

Several tests were conducted to measure the moisture transport rate from the hot water tray at the bottom wall at one end of the chamber to the cold plate at the sidewall of the chamber. For each thermal loading and cold plate temperature, the water condensation rate at the cold plate was recorded after steady state was established within the experimental enclosure. The test results are shown in Table 3-1. The values given in Table 3-1 are averages measured over several hours after steady state temperatures were reached.

Light condensation was observed to form on the inside surface of the chamber along the top wall and the sidewalls after the initial set of tests (Tests 1–3). Starting from the edge of the cold-wall, the top-wall surface covered by condensate spanned a distance of about 0.305 m [12 in]. Closer to the cold plate, higher condensate mass and larger condensate droplet size

Table 3-1. Test Results and Test Conditions. Temperature (Temp.) Sensor Locations (T3–T9) Are Shown in Figure 3-3.								
Test No.	Condensation Rate (ml/hr)	Water Temp. (C)	Cold Plate Temp. (C)	Air Temp-Lower (C)	Air Temp-Middle (C)	Air Temp-Upper (C)	Temp. Top Chamber (C)	Temp. Top Insulation (C)
		T1, T2	T6, T7	T3	T4	T5	T8	T9
1	8.8	38.6	10.7	22.9	26.0	27.2	25.4	23.7
2	16.8	46.1	10.8	26.6	30.2	31.5	29.0	24.1
3	25.6	54.3	10.9	30.9	35.2	36.3	33.1	24.5
4	7.2	32.3	5.3	18.8	21.6	23.2	22.4	24.5
5	12.1	39.4	5.4	21.5	24.9	26.6	24.7	23.1
6	20.9	47.7	5.5	25.1	29.1	30.9	29.0	23.7
7	4.7	25.3	5.2	15.6	17.9	19.2	18.7	23.3
8	2.5	19.5	5.2	14.3	16.3	17.4	18.2	24.2
9	1.7	26.2	19.1	22.6	23.5	24.1	24.0	25.4
10	6.6	38.2	19.1	26.3	28.3	29.5	27.9	25.1
11	20.8	50.9	19.3	32.1	35.3	36.8	34.4	25.1
12	12.8	45.0	19.2	29.2	32.1	33.4	31.5	26.2
13	8.1	46.1	29.5	33.7	35.5	36.6	34.8	25.1
14	4.2	39.7	29.4	31.3	32.2	33.1	31.5	23.9
15	0.5	34.0	29.4	29.7	30.1	30.5	29.6	25.2

was observed. Condensate mass accumulation was also observed on the side walls but the condensation layer did not reach all the way to the bottom of the chamber. A rectangular strip, approximately 0.051 m [2 in] high along the interface between the bottom and side wall, was free of condensation. As condensate formation was observed on the side walls of the chamber in Tests 1–3, an analysis was performed to determine the effect the heat loss from the chamber on condensation. An analysis of the energy balance was performed considering the heater power and the heat loss to the ambient environment. The heat loss through the insulation was estimated using the insulation thickness, chamber surface area, insulation thermal conductivity 0.026 W/m K [0.15 BTU/hr ft °F], and the temperature difference measured across the insulation on the top of the chamber. The amount of water that could condense in the chamber from the heat lost to the ambient environment was estimated from the heat loss rate and the heat of vaporization for water, estimated to be 0.63 W hr/g at 100 °C [975 BTU/lb at 212 °F]. The heat loss rate for Test 3 was estimated to be 5.4 W [18.426 BTU/hr]. This heat loss rate corresponds to a condensation rate of 8.6 ml/hr [0.002 gal/hr] of water. For this test, the measured condensation rate on the cold wall was 25.6 ml/hr [0.007 gal/hr]. Hence the side wall condensation was approximately 29 percent of the cold wall condensation and cannot be neglected. The simplified heat loss analysis, however, neglects any cooling of the water or air in the chamber and assumes all heat loss to the ambient environment results in condensation. The analysis revealed that a significant amount of heat loss was occurring and to reduce it, after Test 3, the shell of insulation surrounding the test chamber was increased to a 0.051-m [2-in] thickness.

Data from Tests 4-15 in Table 3-1 are summarized in Figure 3-4, where the variation of the condensation rate is plotted as a function of the temperature difference between the hot water source and the cooled condensation wall. Four curves, labeled as 5, 10, 20, and 30 °C [41, 50, 68, and 86 °F] curves, represent different absolute temperature regimes in the cold wall plate. Figure 3-4 shows that condensation increases both with the temperature difference

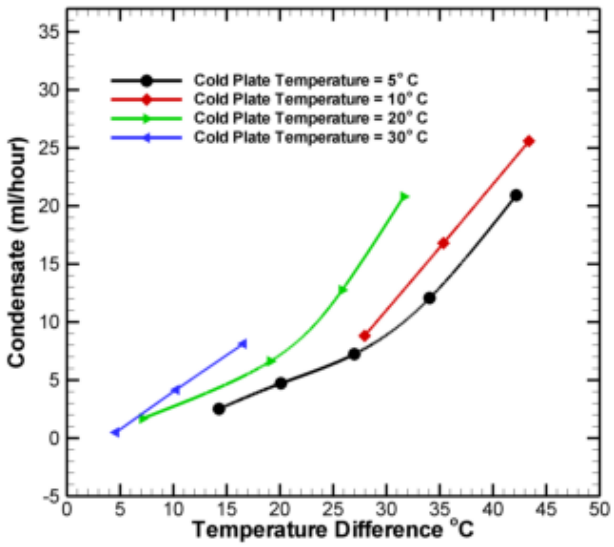

Figure 3-4. Experimental Results Showing the Change in the Condensation Rate As a Function of the Difference Between the Heated Water and Cold Plate Temperatures

between the hot source water and cold condensation plate and also with the absolute temperate regime of the experiment.

3.2 Numerical Modeling of the Moisture Transport Experiments

A numerical model was developed using the commercial CFD package ANSYS-FLUENT Version 12.1 to replicate the experimental study. This general purpose package uses a control-volume-based technique to convert a scalar transport equation to an algebraic equation that is solved numerically. A general description of the package is provided in Chapter 2. Simulation parameters were specifically chosen to suit natural convection flows. The experimental setup was designed to have a single condensation-evaporation cell in a two-dimensional plane with almost no variation in the third dimension. To ensure the two-dimensionality of the flow field, no heat source or sink was placed on the side walls and as mentioned in the previous section, heat loss from the side walls was minimized. Hence a two-dimensional domain was used in the computational study. Rayleigh number calculation indicates that the flow could be transitional or turbulent, depending on the temperature difference between the hot water and cold plate. Hence, resolving turbulence quantities in the flow was deemed important and the two-equation shear stress transport k-ω turbulence model was used in the study.

3.2.1 Numerical Method

General mass transfer modeling techniques used in this study were described in Chapter 2. The experimental study revealed that there were three distinct mass transfer and transport processes that took place within the chamber.

(i) Mass transfer at the walls due to condensation and evaporation that is modeled using suitable boundary conditions

(ii) Transport of evaporated water vapor from the hot source location to the cold wall due to buoyancy driven natural convection

(iii) Condensation of water vapor within the flow domain, where the temperature locally drops below the saturation point

The third process would generate liquid water that will then be transported with the air and water vapor mixture. The quantity of condensed liquid water would be very small, and the effect of this liquid phase on overall gas velocity will be relatively small. The thermodynamic effect, however, could be significant due to latent heat exchange between phases. As mentioned in Chapter 2, the mass transfer at the wall due to evaporation and condensation is modeled using suitable boundary conditions that assume an equilibrium condition at the liquid-water-gaseous mixture interface. This approach also assumes only film condensation occurs (i.e., droplet condensation is excluded). Also, any phase change heat transfer takes place within the wall and does not affect the gas phase. The condensation or evaporation rate is calculated using the water vapor diffusion rate. The volumetric condensation in the domain was simulated using both equilibrium and nonequilibium techniques. The theoretical basis of these techniques and their formulation were described in Chapter 2. The mass transfer boundary conditions at the walls were coded as User Defined Functions and loaded into the solver as surface profiles. The source terms due to mass exchange between phases were added to the mass, momentum and energy equations.

3.2.2 Modeling Results

Figure 3-5 shows the computational grid domain and the boundary conditions of the model. A total of 17,000 nodes were used in the calculation and this grid dimension was determined using a separate grid independence study. It was found that approximately 1.5×10^4 nodes in the domain provided a stable flow field that did not change with grid dimension. Grids were clustered near the wall to capture flow, temperature, and concentration gradients. As discussed in the previous section, a saturation condition was specified at the water source and the cold wall corresponding to the experimental temperature at those locations. The rest of the wall was assigned an adiabatic boundary condition as the heat transfer through those walls was assumed to be negligible.

Simulations were performed for the conditions corresponding to Tests 1–14. The general flow and temperature field data presented here for both the models correspond to Test No. 11 of Table 3-I.

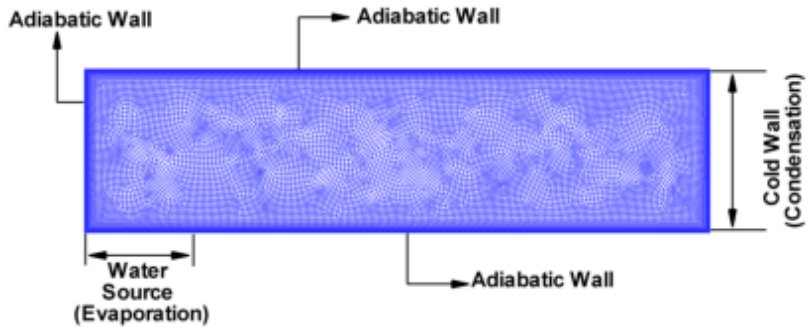

Figure 3-5. Computational Grid and Boundary Condition

Figures 3-6 and 3-7 show the velocity magnitude contours obtained using the nonequilibrium and equilibrium models, respectively. In general, a strong plume is generated from the hot water source that moves upward due to the density difference between the hot and the cold fluid. This plume reaches the upper wall and then moves toward the cold wall. Another high velocity region can be noticed near the cold wall, where the fluid undergoes mass transfer and the colder fluid flows back to the water source creating a cyclic convection pattern that encircles the whole domain. Though there is similarity in the velocity distribution pattern predicted by the two models, the velocity magnitude within the circulation loop calculated by the equilibrium model is higher compared to the nonequilibrium model. This may be attributed to the fact that volumetric condensation has caused a volume deficit in the enclosure that results in a higher velocity of the gas phase.

Figures 3-8 and 3-9 show the temperature field calculated using the equilibrium and nonequilibrium models. A high temperature zone can be identified near the hot water source and the temperature adjacent to the cold wall is lower than the rest of the domain. Though the temperature patterns predicted by both models are qualitatively similar, some difference in magnitude can be noted near the bottom wall of the enclosure. Any difference in the

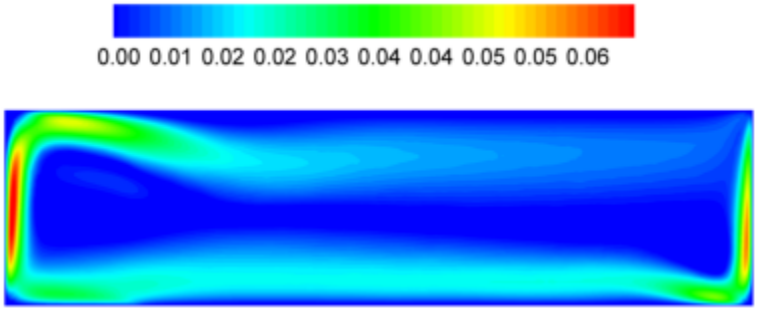

Figure 3-6. Velocity (m/s) Contours Using Nonequilibrium Model (Without Volumetric Condensation) [1 m/s = 3.28 ft/s]

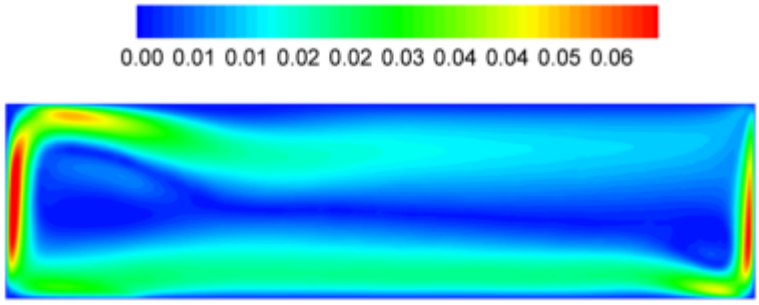

Figure 3-7. Velocity (m/s) Contours Using Equilibrium Model (With Volumetric Condensation) [1 m/s = 3.28 ft/s]

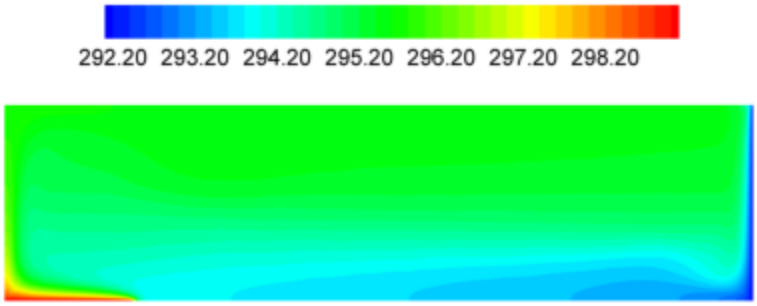

Figure 3-8. Temperature (K) Contours Using Nonequilibrium Model (Without Volumetric Condensation) [°F = 1.8 °K × −459.4]

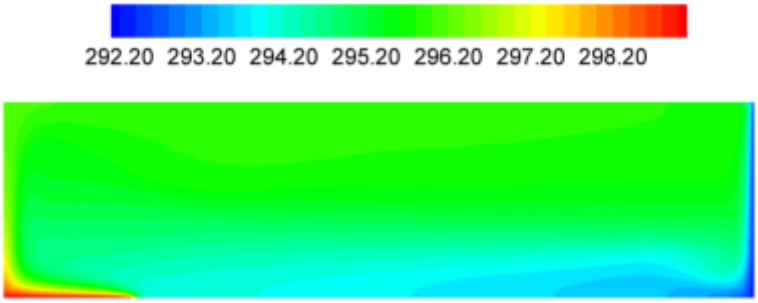

Figure 3-9. Temperature (K) Contours Using Equilibrium Model (With Volumetric Condensation) [°F = 1.8 °K × −459.4]

temperature distribution pattern is solely due to volumetric condensation. The wall evaporation-condensation does not affect fluid temperature inside the domain as latent heat exchange at the wall takes place with the solid material of the enclosure. In general, the temperature distribution pattern is not greatly affected by volumetric condensate formation as the mass of condensate is relatively low. Volumetric condensation, however, can affect localized temperature distribution.

Figures 3-10 and 3-11 illustrate the relative humidity contours of the nonequilibrium and equilibrium models. Note that a substantial part of the domain has relative humidity slightly above 100 percent for simulations that use the nonequilibrium model. This is because supersaturation was allowed in the domain and any possible mass transfer from the air-water-vapor mixture was not considered in the calculation. The equilibrium model shows a different pattern of relative humidity distribution, where the maximum value is capped at 100 percent as any water vapor that contributes to supersaturation condenses to form liquid water. Though supersaturation does not normally occur in an enclosed space, researchers (Brouwers and Chester, 1992a,b; Kang and Kim, 1999; Carey, 2007) have indicated that it can be attained under limited circumstances and the maximum level of supersaturation can be determined using kinetic theory. No experimental measurement was taken for relative humidity in the chamber. As a result, no conclusion on the accuracy of the computed relative humidity pattern using either of the approaches can be made.

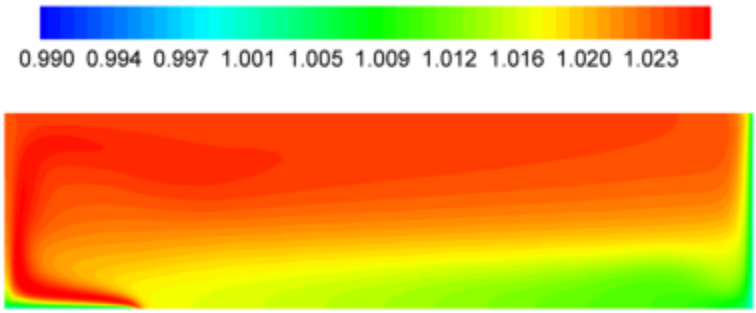

Figure 3-10. Relative Humidity Contours Using Nonequilibrium Model (Without Volumetric Condensation)

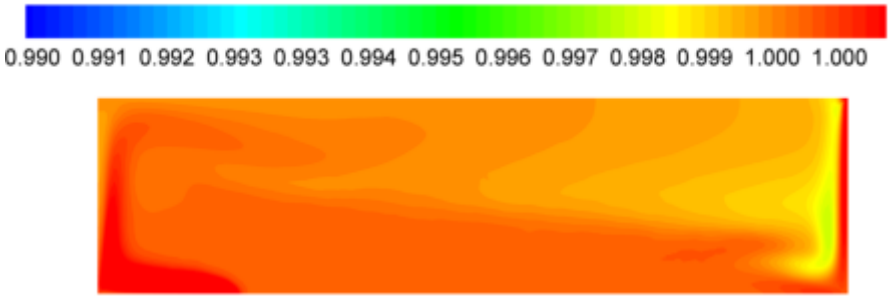

Figure 3-11. Relative Humidity Contours Using Equilibrium Model (With Volumetric Condensation)

The nonequilibium and equilibrium models, however, provide two bounding scenarios as these models consider the minimum and maximum possible water vapor mass that could undergo volumetric condensation.

Figure 3-12 shows the interphase volumetric mass transfer rate for the equilibrium model. The overall volumeric mass transfer rate is small and values are largest in a small region near the hot water source and the cold wall. These regions correspond to high relative humidity zones obtained using the equilibrium model as shown in Figure 3-11. The mass transfer is expected to be maximum in regions where the degree of supersaturation is high. This is because the equilibrium model assumes that mass transfer rate is proportional to the difference between the supersaturation and saturation water vapor concentrations.

3.2.3 Comparison Between and Experimental and Computed Data

Figures 3-13 and 3-14 show the comparison between experimentally obtained and computed condensation rates using the nonequilibrium and equilibrium models, respectively. The data are grouped together in four distinct sets that correspond to different convection regimes mentioned in Section 3.1.2. Generally, both computed data sets matched the trend of the experimental data, where the condensate rate increases with increased temperature difference.

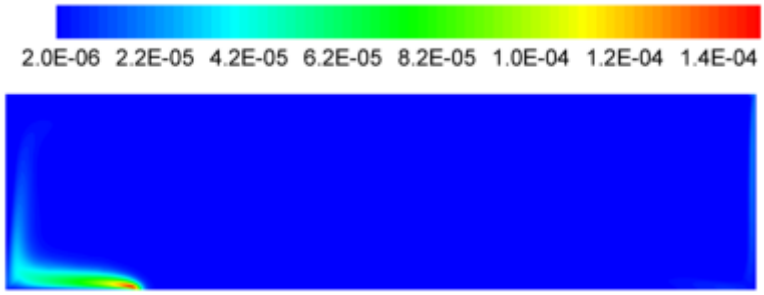

Figure 3-12. Interphase Mass Transfer (kg/m^2-s) [1 kg/m^2-s = 0.205 lb/ft^2-s] Due to Volumetric Condensation Using Multiphase Flow

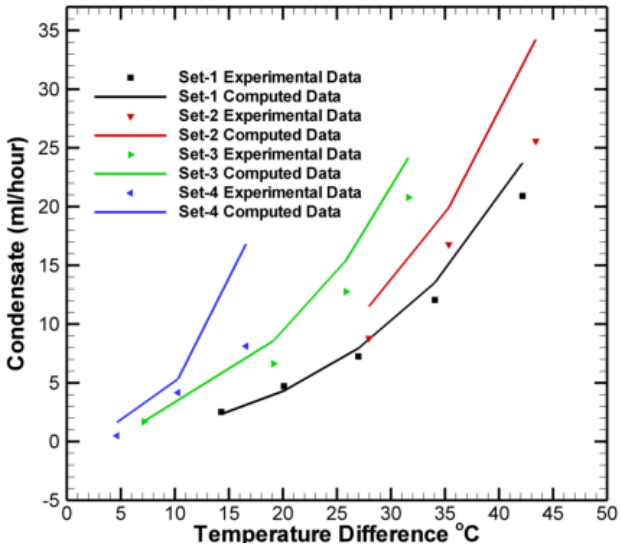

Figure 3-13. Comparison of Experimental and Computed Values of Condensation Rate Using Nonequilibrium Model (Without Volumetric Condensation) [1gal/hr = 3785.41 ml/hr; °F = 1.8 × °C + 32]

Though both models overpredict condensation rate, a closer examination of the results shows that the computed results using the equilibrium model match the experimental data better, especially at a lower temperature difference. For example, the lower water vapor content in the gaseous mixture near the cold wall (using the equilibrium model) is lower than the corresponding values obtained using nonequilibium model. This is because some of the water vapor available within the mixture has already been allowed to condense and form liquid mist in the equilibrium model. On the other hand, the entire water vapor content is convected from the hot water pool to the cold wall in the nonequilibium model calculations resulting in a higher wall condensation rate.

Figures 3-13 and 3-14 also establish the effect of the temperature difference between the cold and hot wall in total mass transfer rate across the domain. The quantity of water evaporating at the hot surface depends on the temperature difference between the hot water pan and the bulk

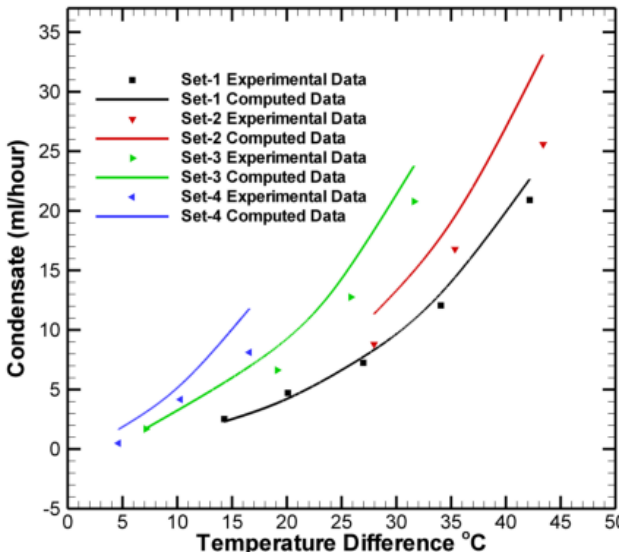

Figure 3-14. Comparison of Experimental and Computed Values of Condensation Rate Using Equilibrium Model (With Volumetric Condensation) [1gal/hr = 3785.41 ml/hr; °F = 1.8 × °C + 32]

temperature. On the other hand, the condensation rate depends on the temperature difference between the cold plate and the bulk fluid (air). Under steady state conditions, the rate of condensation will be equal to the rate of evaporation. In essence, the air temperature will adjust so that the condensation and evaporation rates are the same. At this condition, the entire condensation-evaporation cycle will depend only on the temperature difference between the hot and cold plates, irrespective of the temperature distribution of air.

Figures 3-15 and 3-16 show the temperature comparison at thermocouple locations T3, T4, and T5 as indicated in Figure 3-3 for sets 1, 3, and 4. Only three sets of data are presented for clarity. The majority of the temperature data have been underpredicted by the nonequilibrium model, whereas the match between the experimental and computed data is better for the equilibrium model. As with the case of condensation rate, the better match using the equilibrium model can be attributed to including volumetric condensation, which is not considered in the nonequilibrium model. Consequently, any thermal effect due to exchange of latent heat is not accounted for in the nonequilibrium model. In reality, condensate water releases the latent heat in the continuous flow resulting in a higher temperature forthe gas phase. This phenomenon is accounted for in the equilibrium model, where the latent heat of condensation is absorbed by the gas mixture resulting in a higher temperature that is closer to the experimental observation.

3.3 Summary

This chapter discussed a combined experimental and computational study to understand the condensation-evaporation cycle in an enclosed space. The primary objective of the study was to verify and benchmark the numerical technique described in Chapter 2 for further use in simulating multiphase natural convection dominated cold-trap process. The experimental study explore the effect of volumetric condensation. The results presented showed the velocity, temperature, and relative humidity distribution of the system. It was observed that the

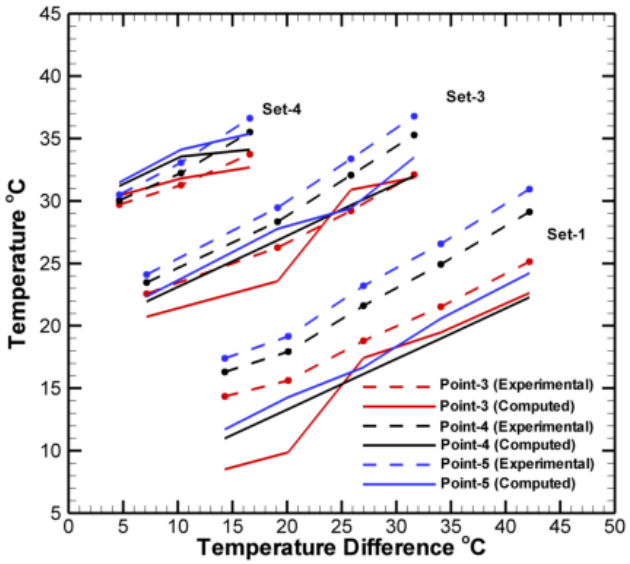

Figure 3-15. Comparison of Experimental and Computed Values of Temperature Using Nonequilibrium Model (Without Volumetric Condensation) [°F = 1.8 × °C + 32]

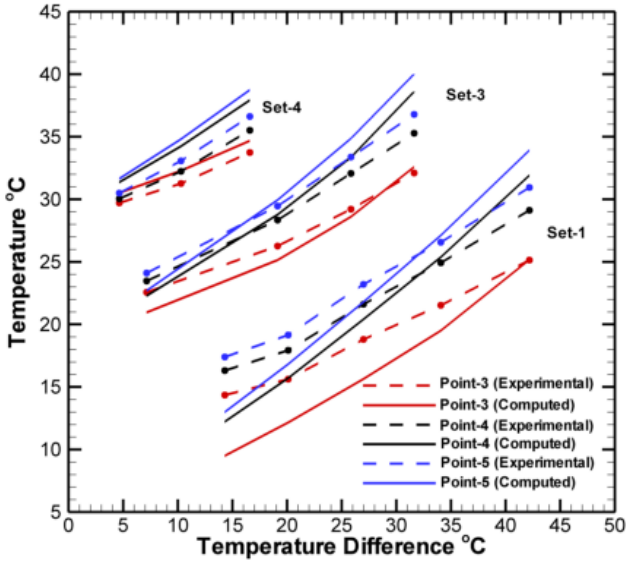

Figure 3-16. Comparison of Experimental and Computed Values of Temperature Using Equilibrium Model (With Volumetric Condensation) [°F = 1.8 × T °C + 32]

was conducted in a closely controlled environment, where a condensation-evaporation cycle was created within an enclosure using a water source and cold plate at constant temperatures. The experimental study was conducted for a range of temperature differences between the cold plate and hot water source. Subsequently, a numerical study was conducted to simulate the experimental setup. The numerical methodology described in Chapter 2 was used to replicate the experiment. Both nonequilibrium and equilibrium multiphase models were studied to

equilibrium model predicted moisture content level bounded by saturation limit unlike the nonequilibrium model that predicted supersaturation. Numerical results of the condensate rate using both models matched the general experimental trends and patterns, but the equilibrium model provided a better prediction due to the availability of additional water vapor at the cold wall. Similarly, the numerical simulations provided temperature distributions that compared well with experimental observations. However, the equilibrium model provided a better match as compared to the nonequilibium model. The temperature values computed using the nonequilibrium model were lower as it ignored the latent heat absorption due to volumetric condensation process.

4 20-PERCENT SCALE MODEL OF A DRIFT

This chapter describes an experimental and numerical study conducted using a 20-percent drift-scale configuration. The objective of the experimental study was to gain insights into the cold-trap process and provide measured data for benchmarking and validating the computational fluid dynamics (CFD) simulations. The data collected from the experiments in the 20-percent drift-scale also provided boundary and initial conditions necessary to perform the numerical analysis. Details of the experimental setup and experimental results are documented in Manepally, et al. (2006) and Green (2010).

There are a number of significant differences between the experimental and benchmarking exercise described in Chapter 3 and the study described in this chapter. The condensation-evaporation cell experiment described in the previous chapter was conducted in a closely controlled environment, with minimum heat loss to the environment and stringent monitoring of the water source and cold plate temperatures. The condensation cell was also configured such that a single two-dimensional convection cell in the vertical plane would form within the enclosure. There was little cross flow or heat exchange in the horizontal plane. Hence a two-dimensional numerical simulation along the central vertical plane was sufficient to model the problem. On the other hand, the 20-percent drift-scale experiment was conducted in a relatively open environment to replicate the actual atmosphere of an underground drift. The experimental set-up contained a closed thick cylinder, but no special effort was made to restrict heat and mass transfer between the experimental system and the surroundings. The flow and heat transfer were also expected to be strongly three-dimensional with cross flow convection and heat transfer. Another significant difference between the convection cell experiment and the 20-percent drift-scale study lies in the mode of heat transfer. Due to relatively low temperature difference between the hot water and cold plate, radiation heat transfer was not significant in the previous study as described in Section 3. However, in the 20-percent drift-scale experiment, radiation heat transfer plays an important role. Overall, the focus of the benchmarking study in this chapter is to assess the capability of the CFD model in simulating the flow and thermal environment, including the cold-trap process in an emplacement drift

4.1 The 20-Percent Drift-Scale Experiment

The experimental setup design and results are discussed in this section. Two distinct sets of experiments were conducted. In the first set, the temperature variation due to natural convection was studied without any moisture transport. The second set included the effect of moisture transport and measured the temperature and relative humidity in the domain.

4.1.1 Design of the Experiment

The experimental setup consists of a polyvinylchloride pipe (PVC) closed on each end to simulate the enclosed environment and four aluminum analog waste packages as shown in Figure 4-1. The pipe that simulates the drift walls is approximately 6.51 m [21.35 ft] in length, with internal and external diameters of approximately 1.06 m [3.48 ft] and 1.134 m [3.72 ft], respectively. The end caps on the pipe are made of 1.3 cm [0.5 in] thick low thermal conductivity Lexan® to minimize heat loss and allow visual observation of the experiment.

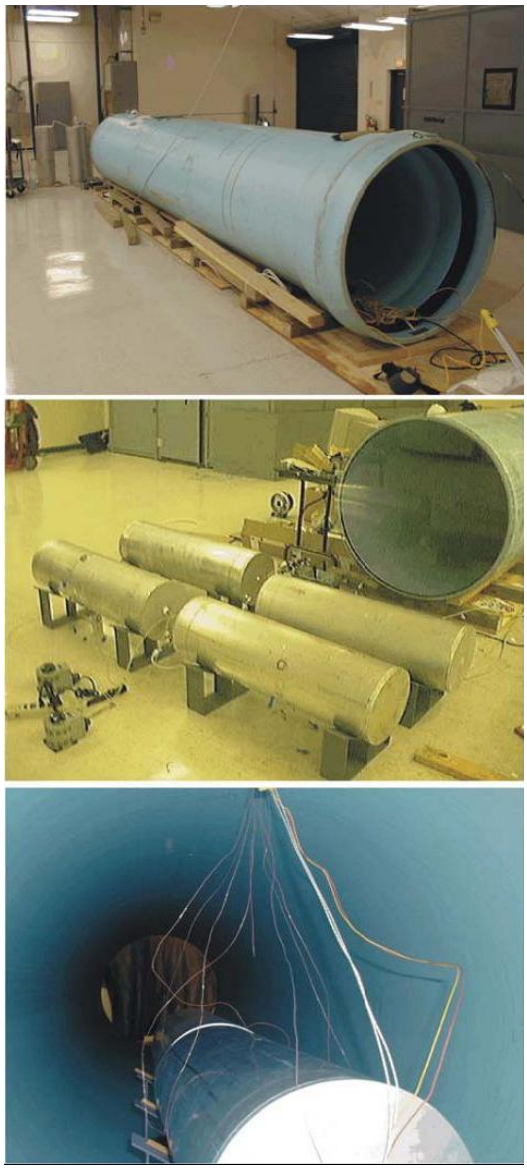

(a)

(b)

(c)

Figure 4-1. Photographs of the 20-Percent Scale Drift Natural Convection and Cold-Trap Laboratory Model With (a) Polyvinylchloride Pipe, (b) Four Analog Waste Packages and Stands, and (c) Waste Packages Inside the Pipe With Thermocouples to Measure Surface Temperature

Figure 4-2 shows the 20-percent drift-scale pipe geometry and dimensions. The axial cross section of the pipe shows the offset of the waste packages placed eccentrically into the drift pipe and separated by a constant distance of 5 cm [2 in] from the left end of the pipe (hot end wall) and between adjacent waste packages. The extreme ends of the pipe were sealed to minimize the flow of air in and out of the pipe. The end cap of the pipe closest to the waste packages will be referred to as the hot end wall throughout this report; likewise, the other end cap which is far away from the waste packages is called the cold end wall.

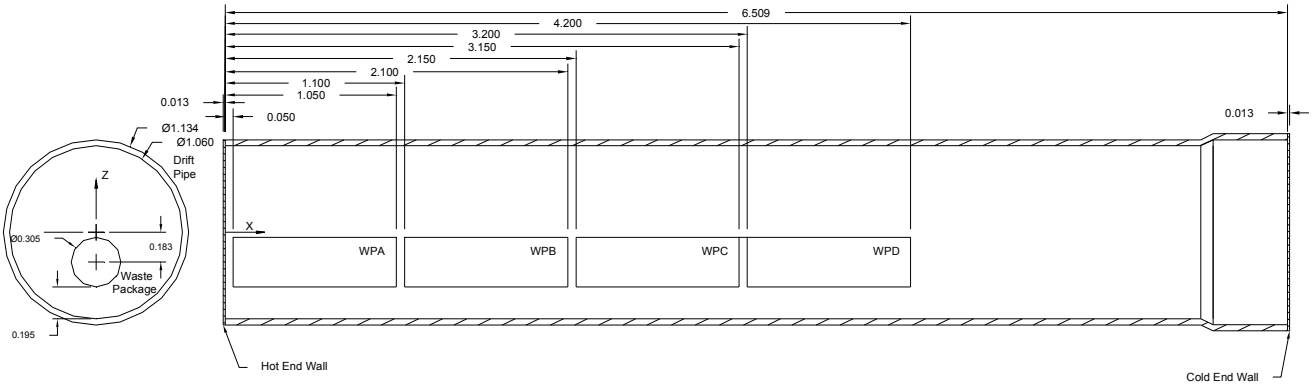

Figure 4-2. Schematic Drawing of the 20-Percent Drift-Scale Laboratory Model. Longitudinal Cross Section Shows the Length of the Tube and Waste Packages and Their Location Relative to the Hot End Wall. Four 20-Percent Scale Waste Packages (WPA, WPB, WPC, and WPD) Are Placed Eccentrically in the Z-Direction. Dimensions Are in Meters. [1 m = 3.28 ft]

Four waste packages are used to simulate the effects of uniform and non uniform heat loads on the evolution of the cold-trap process. Each waste package is approximately 30.5 cm [12 in] in diameter and approximately 1 m [3.28 ft] in length. Extending internally from one face of each waste package is a heating rod. During the experiments, the rod is heated in the presence of a vacuum pressure of 689.5 Pa [0.1 psia] inside the analog waste package so that radiation is the dominant heat transfer process between the rod and the walls resulting in uniform heating of the waste packages.

For tests with moisture, water was introduced inside the PVC through tubing located right above the waste package closest to the hot end (Figure 4-2). Paper towels were located on the top of the first waste package (WPA) to (i) distribute the liquid on the surface of the waste package, (ii) avoid water dripping off the waste package, and (iii) enable observation as the experiment progressed (Figure 4-3).

4.1.2 System Monitoring

During the experiments, the temperature was monitored using 120 nested calibrated thermocouples on the surface of the waste packages, suspended in the air, and on the inner and outer walls of the pipe. These thermocouples were placed in different axial locations that are shown in Figure 4-4(a). Each cross section location was instrumented to obtain a comprehensive map of the temperature field. An example of the location of thermocouples in a cross section of the pipe is shown in Figure 4-4(b). Detailed information on the location of the thermocouples can also be found in Manepally, et al. (2006).

In the following sections of this report, the term “cross sectional average temperature” will refer to the average of the individual measured or simulated air temperature values at the different locations in a cross section as shown in Figure 4-4a. The number of points in each cross section was based on preliminary CFD simulations. Sensors were located in areas where significant fluid (air) movement and/or temperature gradients were anticipated.

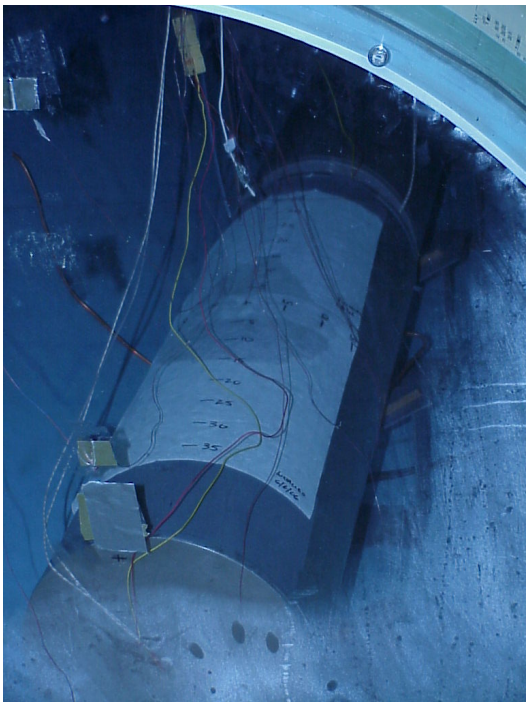

Figure 4-3. Photograph of Moist Area on Top of Waste Package A During Experiments With Moisture

During the testing with moisture, temperature was monitored using thermocouples and thermistors. Relative humidity was monitored using a series of sensors at 15 different locations along the centerline of the drift and at different heights. The humidity measurements were made with commercially available humidity sensors.

4.1.3 Experimental Conditions

The thermal and air flow field within the experimental setup were expected to change with time. The use of constant boundary conditions and heat rates, however, allowed the system to reach a point where average in-drift parameter change was negligible as compared to the initial transient response at the beginning of the test. Hence, all of the experimental measurements were taken after the initial transient period was over and the system had reached a steady state.

As mentioned previously, two main scenarios were considered in the testing. For the first scenario, the drift was instrumented as described in Section 4.1.2, and cap ends were installed at each end of the pipe isolating the ambient air within the pipe from the rest of the room. However, as no water was introduced internally, 'dry' is used here to identify any experimental or numerical results obtained under this first scenario. Only temperatures were measured for the 'dry' cases.

The second scenario involved adding water inside the 20-percent drift-scale pipe to represent a potential source of liquid in the drift. Liquid water was added on top of the waste package closest to the hot end wall (Figure 4-3). During testing, temperature and relative humidity

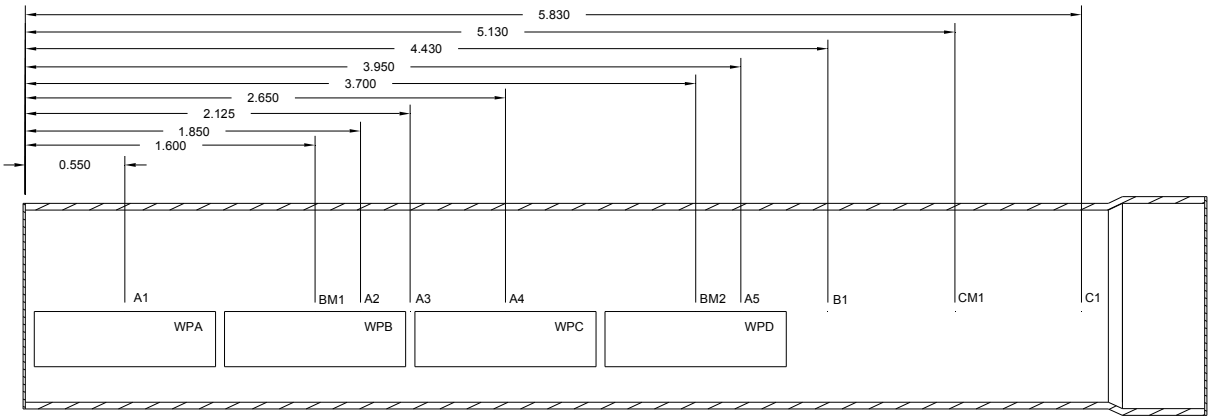

(a)

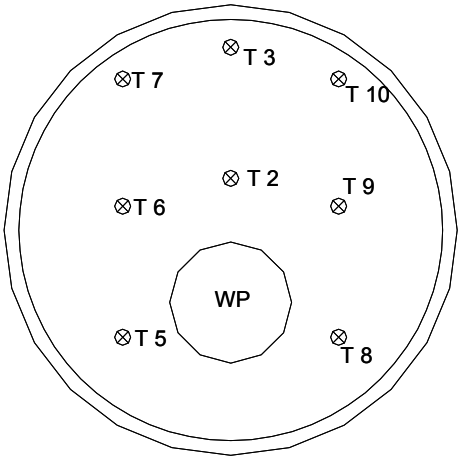

$$\text{Cross} - \text{sectional average} = \frac{T2 + T3 + T5 + T6 + T7 + T8 + T9 + T10}{8}$$

(b)

Figure 4-4. (a) Schematic Showing the Location of Axial Planes Selected for Placing Thermocouples and (b) Example Location of Thermocouples at a Cross Section and Calculation of the Cross Sectional Average Air Temperature

were measured at different locations. This part of the analysis aids in understanding both temperature and moisture redistribution along the 20-percent drift-scale model. The results and analyses related for the second scenario are identified by 'moist' in the following sections of this report.

Four different combinations of heating rates applied to the waste packages were selected to investigate the effect of the total heat load and distribution on the cold-trap process inside the drift pipe (Table 4-1). The nomenclature in Table 4-1 is used in the following sections of this report to identify the different configurations of heat load distribution applied during the testing and CFD analysis. The four different heat load distributions shown in Table 4-1 were used during the tests with dry air, and only two cases, one with uniform {50 W [170.6 BTU/h]} and one with nonuniform heat distributions {75-25-25-75 W [266-85-85-266 BTU/h]}, were employed during the tests with moisture.

Table 4-1. Thermal Loads for the 20-Percent Scale Experiments							
Waste Package	**WPA**	**WPB**	**WPC**	**WPD**	**Total Heat Rate (W)***	**Nomenclature**	**In-Drift Fluid Condition: Moist (M)† and Dry (D)‡**
Uniform Heating Rate (W)*	50	50	50	50	200	50 W	M and D
	75	75	75	75	300	75 W	D
Non-uniform Heating Rate (W)*	75	25	25	75	200	75-25-25-75 W	M and D
	80	60	40	20	200	80-60-40-20 W	D

*1 W = 3.4 BTU/h
†M indicates that both temperature and relative humidity were measured during testing and the User Defined Functions for volumetric condensation, wall condensation and evaporation in ANSYS-FLUENT® were used in the numerical simulations.
‡D also implies that only temperatures were measured during testing and the baseline ANSYS-FLUENT® solver was used without any User Defined Functions.

4.1.4 Experimental Results

The majority of the experimental results are discussed along with numerical data in Sections 4.2.2.1 and 4.2.2.2. Some highlights of the experimental data are shown in Figure 4-5. A plot of the cross sectional average temperatures as a function of the distance along the drift is shown in Figure 4-5 for different variants of thermal loads. Average temperatures are always higher for the uniform heating case 75 W [266 BTU/h] as the total heat load {300 W [1,024 BTU/h]} is higher than for the three other cases {200 W [682 BTU/h]}. All the temperature curves resulting from the 200 W [682 BTU/h] thermal load converge towards a single value toward the cold end of the drift. However, the 75 W [266 BTU/h] case shows a higher temperature value at drift-end. There is, however, substantial variation in the temperature pattern over the waste packages due to the difference in thermal load distribution, although the total heat load is the same. In general, there is a decrease in temperature from the hot end toward the cold end on the order of 2–4 °C [3.6–7.2 °F].

4.2 The 20-Percent Drift-Scale Modeling

The numerical model developed using ANSYS-FLUENT (ANSYS, Inc., 2009a) for simulating the 20-percent drift-scale experiment is described in this section. Temperature, relative humidity, and velocity contours computed from the model are presented at different cross sectional locations. Numerical results are also compared with experimental data for average temperature and relative humidity values at specific locations.

4.2.1 Model Development

A detailed three dimensional model was developed for the 20-percent drift-scale experimental setup using ANSYS-FLUENT. The immediate objective of this exercise was to benchmark and

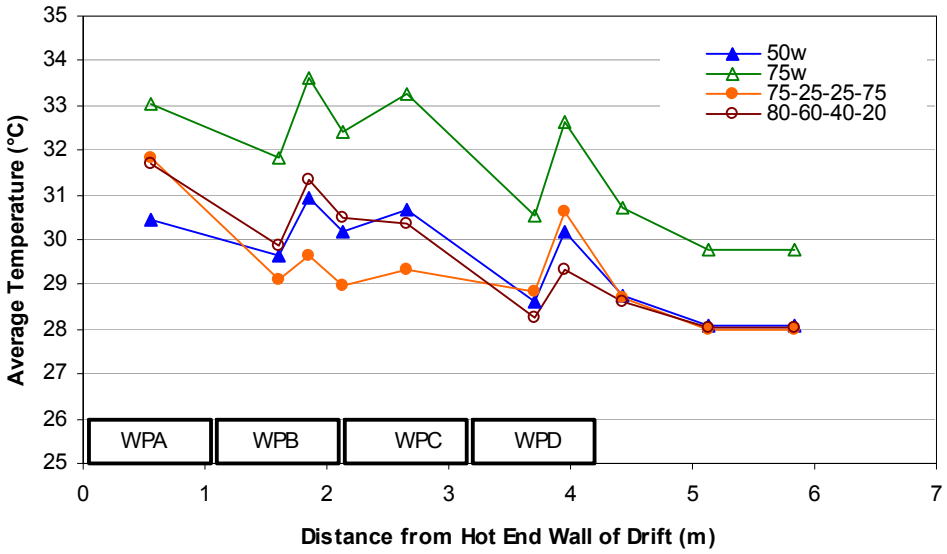

Figure 4-5. Observed Average Cross Sectional Air-Temperature Profile for All the Dry Cases With Different Heat Load Distributions Between Individual Waste Packages [1 m = 3.28 ft; °F = 1.8 x °C + 32; 1 W = 3.4 BTU/h]

verify the developed User Defined Functions (UDFs) for modeling condensation. The broader objective was to assess the general numerical approach for its intended use in simulating the cold-trap process.

The computational domain used in the model is shown in Figure 4-6. Some of the dimensions and boundary conditions are also highlighted in Figure 4-7. The outer boundary of the domain is a cylindrical surface of 0.53 m [1.738 ft] diameter and a thickness of 0.023 m [0.007 ft], that represents the drift. A numerical study was conducted to see the effect of the outer wall boundary condition on the temperature distribution pattern. Two different boundary conditions were tested: (i) a specified temperature at the outermost surface and specified wall thickness, where the PVC pipe shell was not included in the computation and (ii) a convective flow boundary condition at the outermost surface with a specified ambient temperature, where the pipe thickness was included in the computation. It was observed that a convection boundary condition on the outermost surface of the PVC pipe provided the best estimate and this approach was adopted for rest of the modeling exercises. The ambient temperature used in the calculation was obtained from the experimental observations.

The emplaced 20-percent scale waste packages have a length of 1 m [3.28 ft] and a diameter of 0.365 m [1.198 ft]. The waste package volumes were included in the computation. It was assumed in the computation that the waste packages were solid objects with a uniform thermal conductivity and has a uniformly distributed constant volumetric source. The thermal load specified in the waste packages was in accordance with the experimental input and was varied for different tests to reflect the loading used in the experiment. The air density was calculated using a Boussinesq approximation which assumes that density is a function of temperature and

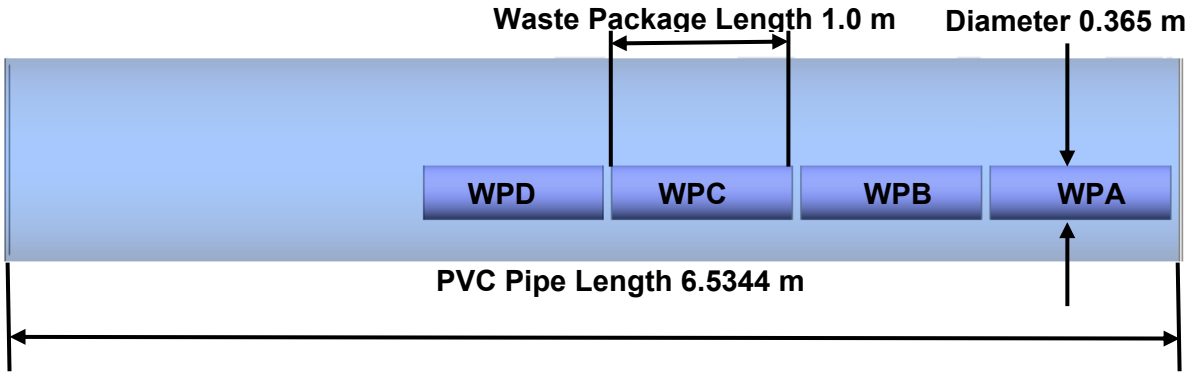

Figure 4-6. Schematic of the Three-Dimensional ANSYS-FLUENT® Model Showing Relevant Dimensions [1 m = 3.28 ft]

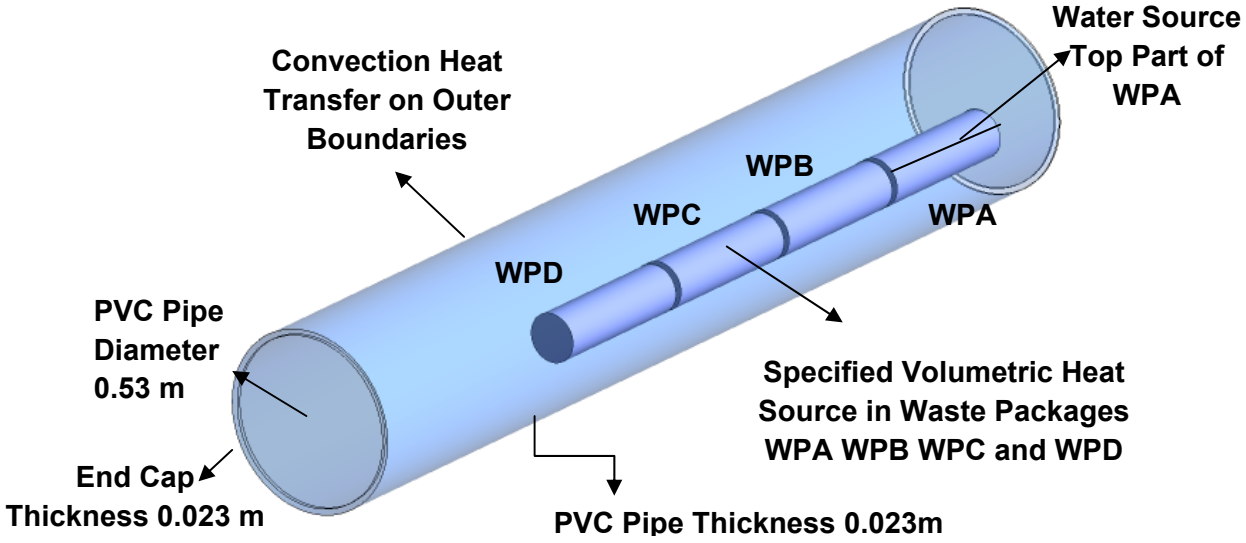

Figure 4-7. Schematic of the Three-Dimensional ANSYS-FLUENT® Model Showing Dimensions and Boundary Conditions [1 m = 3.28 ft]

is independent of pressure. This assumption is valid as the flow velocity was expected to be low and variation in pressure was expected to be minimal. The 'dry' and 'moist' air properties used in the calculation werw obtained from Incropera and DeWitt (1996) and Reynolds (1979).

The mesh elements used in the model are shown in Figure 4-8. Mostly hexahedral elements are used to increase computational efficiency, but some tetrahedral elements were needed to effectively mesh small gaps. Figure 4-9 shows the mesh elements used for the waste packages and end caps. It also highlights the cross sectional distribution of the mesh. A weep algorithm was used to generate the volumetric mesh from a surface distribution. As shown, a finer mesh resolution was used near the solid walls to resolve hydrodynamic and thermal boundary layers.

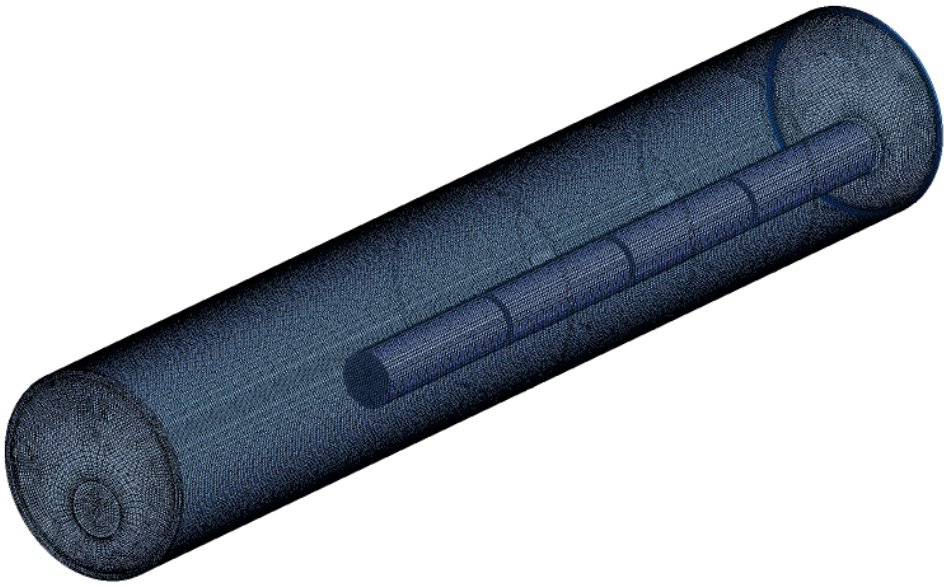

Figure 4-8. Volumetric Mesh for the Computing Domain Used in the ANSYS-FLUENT® Model

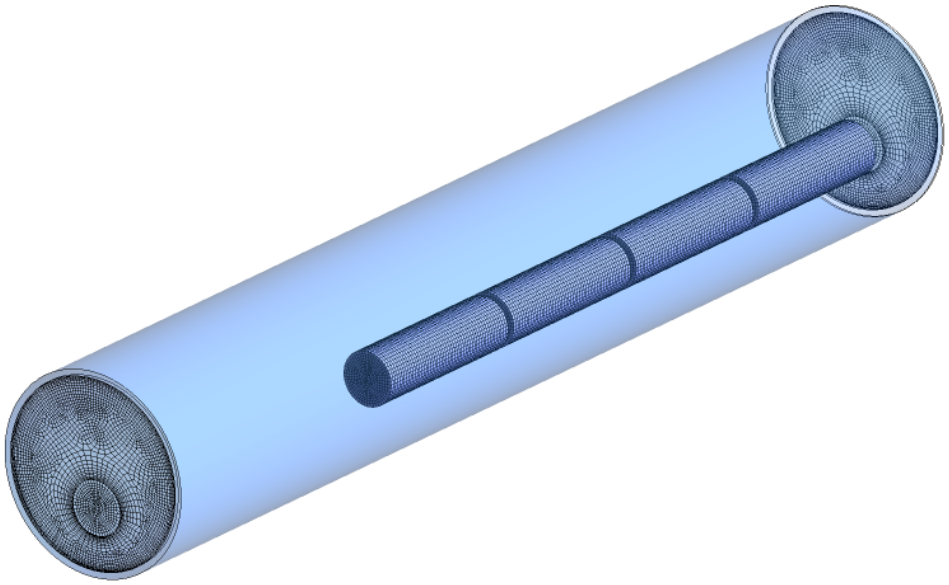

Figure 4-9. Highlight of Meshing Over Waste Packages and End Caps Used in the ANSYS-FLUENT® Model

4.2.2 Model Results

Modeling results are presented in two sections. Section 4.2.2.1 presents results for the 'dry' cases, where no liquid water was available for evaporation. All four scenarios for the thermal loading described in Table 4-1, which includes two uniform {50 and 75 W [170.6 and 266 BTU/h]} and two nonuniform {75-25-25-75 and 80-60-40-20 W [266-85-85-266 and 273-205-137-68 BTU/h]} heat load distributions, were simulated. For the 'dry' cases, all three modes of heat transfer, conduction, convection and radiation were included in the model. As mentioned in Section 2.3, the discrete ordinate model was used to calculate radiation. Temperature contours and velocity vectors at different cross sectional locations are presented for the 'dry' case with a 50 W [170.6 BTU/hr] thermal load. In addition, cross section averaged temperature values from the computed data are compared with available experimental data for all the simulated runs.

Section 4.2.2.2 presents results for the 'moist' case where a source of liquid water was specified to exist on the upper half of the waste package WPA outer surface and was available for evaporation. As indicated in Table 4-1, two different thermal loading scenarios were considered for the 'moist' case; one uniform loading of 50 W [170.6 BTU/hr] and one nonuniform loading of 75-25-25-75 W [266-85-85-266 BTU/hr]. For the 'moist' cases, relative humidity and temperature distributions at different cross sectional locations are presented with a 50 W [170.6 BTU/hr] thermal load. Also, the section averaged temperature and relative humidity data obtained from the simulation are compared with the experimental results for all the simulated runs.

4.2.2.1 Simulation of Dry Cases

Figures 4-10(a) and (b) show the streamlines obtained from the 50 W [170.6 BTU/hr] 'dry' simulation case. The streamline ribbons track the flow path and the colors indicate velocity magnitude. The streamlines highlight the general velocity pattern generated due to buoyancy driven natural convection. In general, a large axial circulation loop can be observed from both Figures 4-10(a) and (b). In this loop, air moves from the hot to the cold end of the drift in the space above the waste packages. Air convects back from the cold to the hot end through a gap between waste packages and the bottom wall. Streamlines in Figure 4-10(a), however, also indicate the three dimensionality of the flow field, due to the presence of strong vertical currents in planes between waste packages. Away from the waste packages, towards the cold end of the tube, the flow is mostly in the axial direction and exhibits a two dimensional pattern that is mostly highlighted in Figure 4-10(b).

Axial velocity magnitude contours and velocity vectors at different cross sectional planes will help to further explore the pattern of the velocity distribution in different regions. Figure 4-11 is a schematic that shows different cross sectional planes, where velocity and temperature contours are presented.

Figures 4-12 through 4-16 show the velocity distribution in the cross sections defined in Figure 4-11 for four different thermal loading conditions. The contours in these diagrams represent axial velocity magnitude. Figure 4-12 shows the results for the 50 W [170.6 BTU/hr] uniform thermal loading scenario and will be discussed here as the baseline result. It is clear from the vector plots of axial planes 1 through 4 that due to the thermal effect, strong velocity plumes are created around the waste packages that convect in the vertical direction. This finding agrees with the experimental observations of Kuehn and Goldstein (1976 and 1978), where they

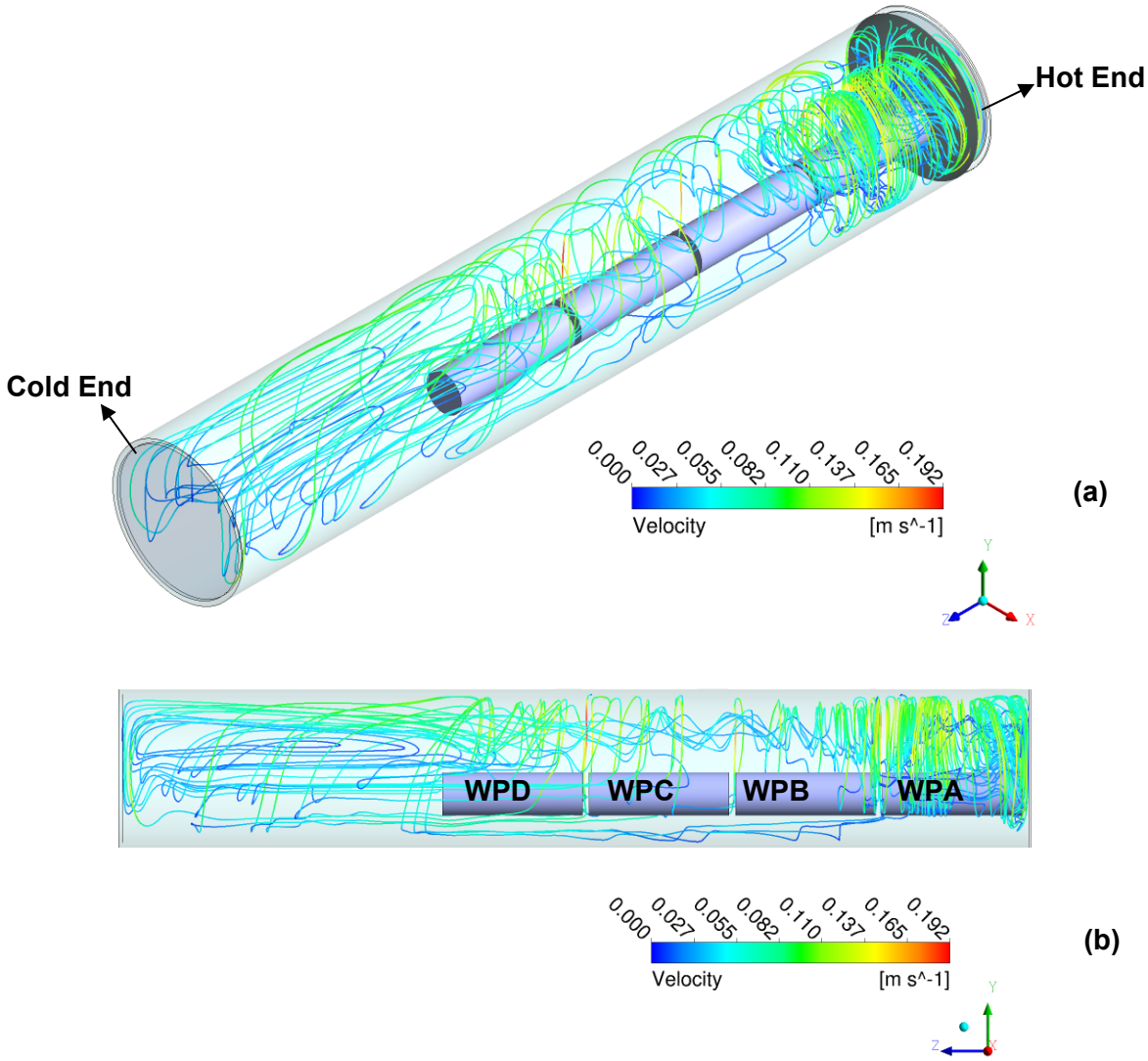

Figure 4-10. Airflow Streamlines for a Uniform 50 W [170.6 BTU/hr] Heat Load [1m/s=3.28 ft/s]

observed a similar flow pattern. The velocity distribution pattern in the vertical YZ plane confirms the existence of these vertical convection currents and also highlights the two dimensional flow pattern away from the waste packages towards the cold end of the tube. A high axial velocity region near the top surface can be observed in the vertical YZ plane after the flow leaves the waste package WPD. The combined air mass that convected vertically upwards due to the thermal effect of the waste packages, tends to move axially once it leaves the waste package area and creates a high velocity region.

Figures 4-13 through 4-15 highlight the effect of uniform and nonuniform thermal loading on the velocity distribution pattern. As is clear from Figure 4-13, the high load waste packages {75 W [266 BTU/hr] for WPA and WPD} creates a stronger vertical movement evident from the higher velocity magnitude compared to the low load waste packages {25 W [85 BTU/hr]} for WPB and WPD). Similar observations can be made in Figure 4-15, where the largest vertical velocities are observed above WPA that has the maximum heat load of 80 W [275 BTU/hr] and the

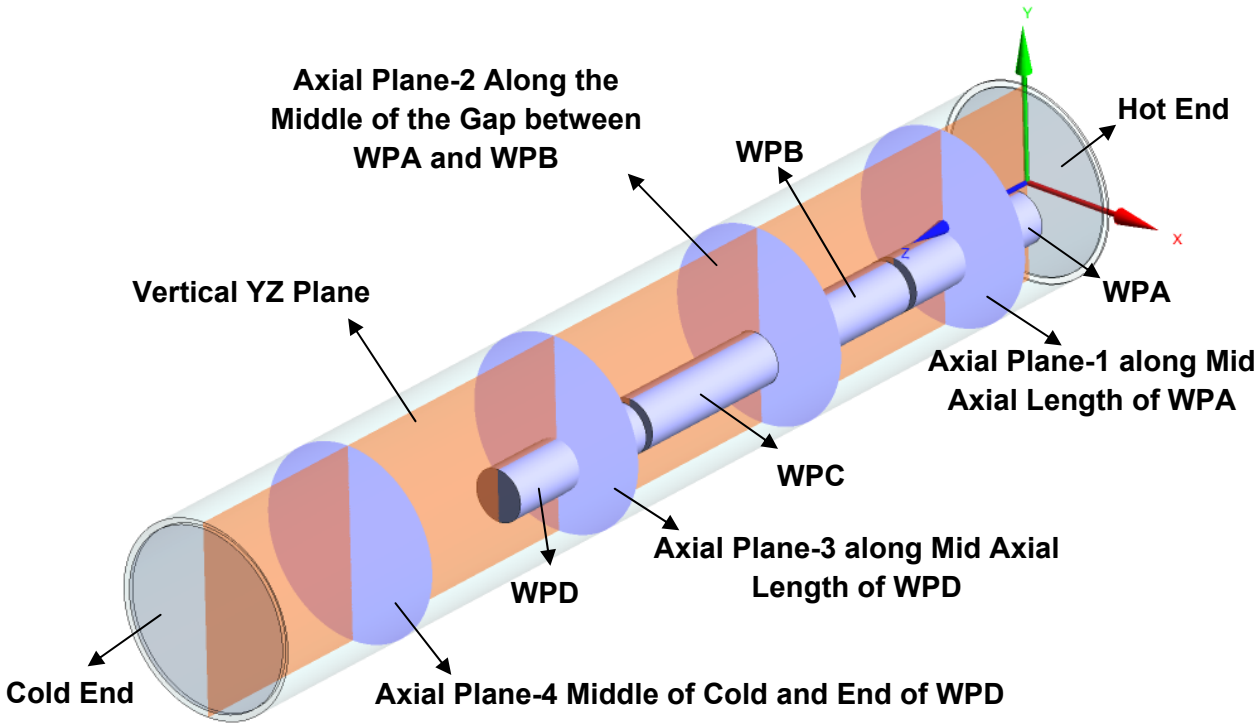

Figure 4-11. Schematic of Cross Sectional Planes

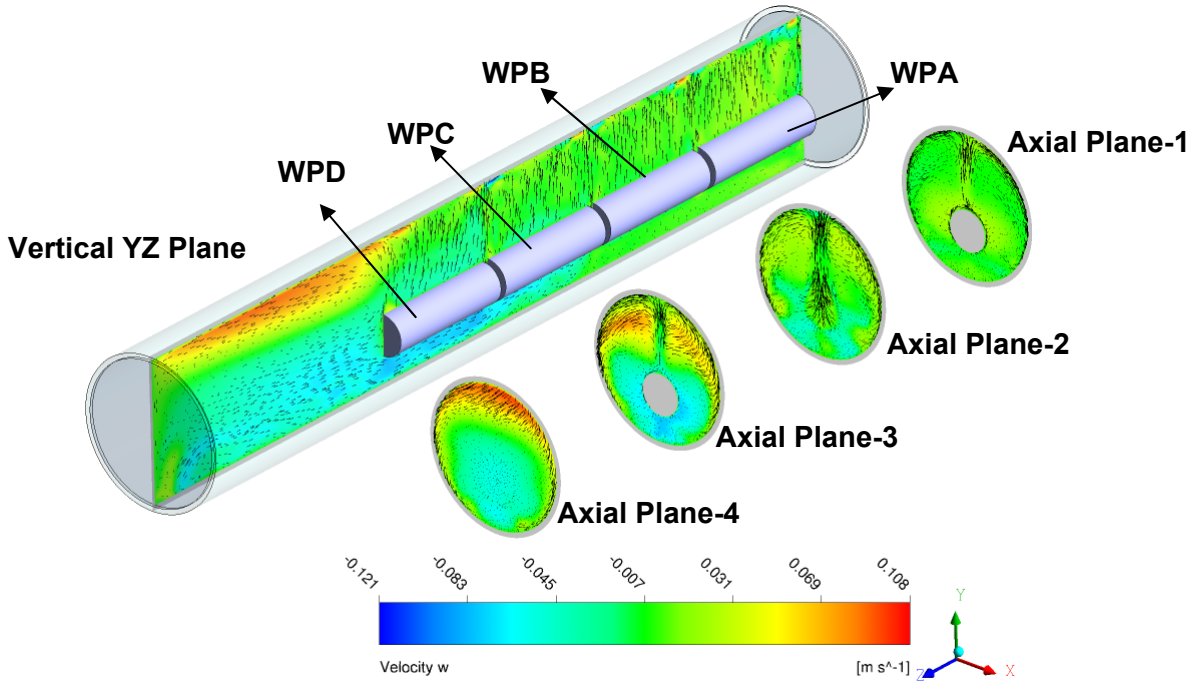

Figure 4-12. Velocity Vectors and Axial Velocity Contours for the Dry Simulation With a Thermal Load of 50 W [170.6 BTU/hr; 1m/s=3.28 ft/s]

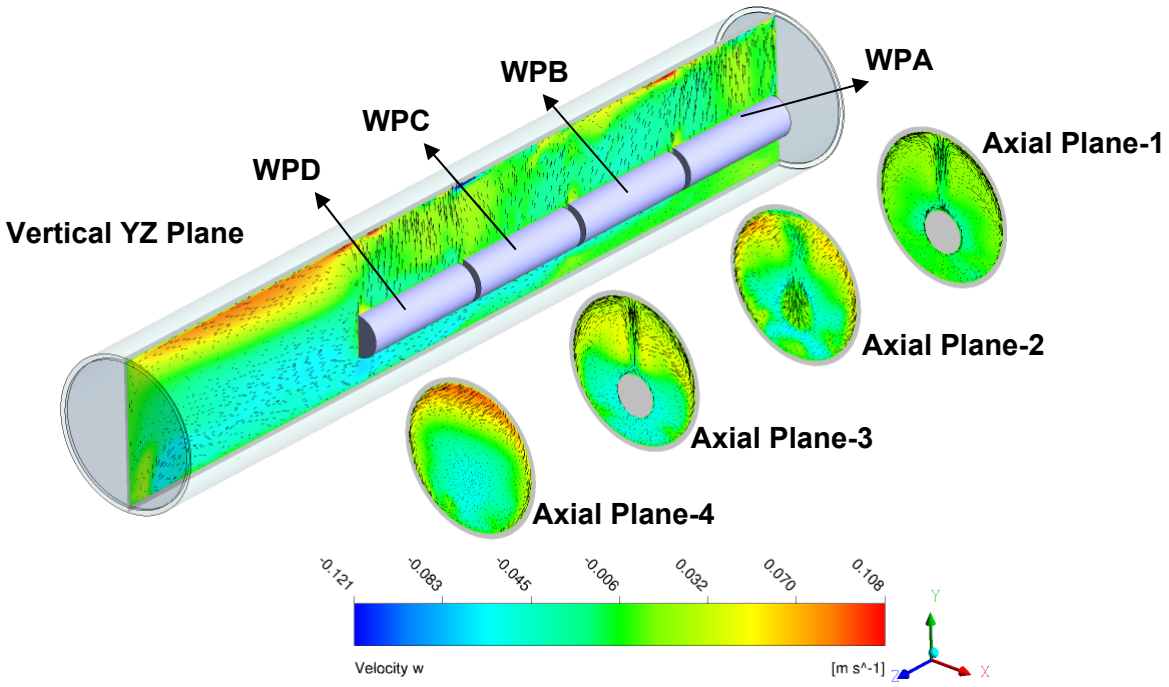

Figure 4-13. Velocity Vectors and Axial Velocity Contours for the Dry Simulation With Thermal Loads of 75-25-25-75 W [266-85-85-266 BTU/hr; 1m/s=3.28 ft/s]

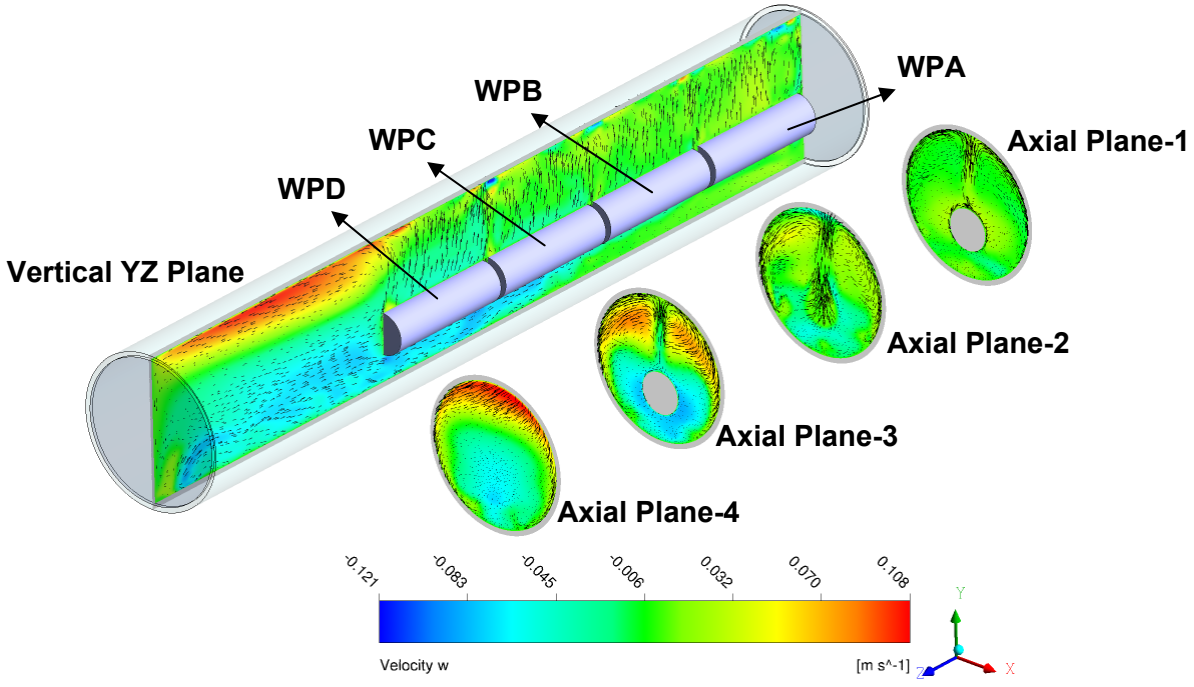

Figure 4-14. Velocity Vectors and Axial Velocity Contours for the Dry Simulation With a Thermal Load of 75 W [266 BTU/hr; 1m/s=3.28 ft/s]

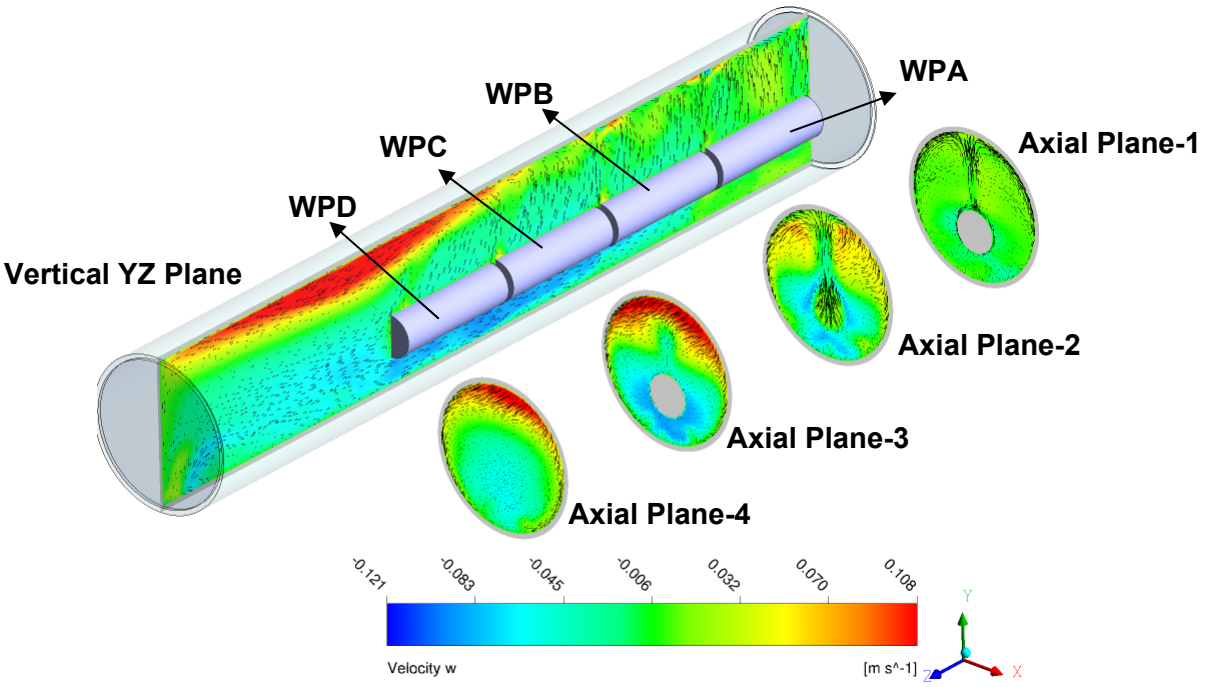

Figure 4-15. Velocity Vectors and Axial Velocity Contours for the Dry Simulation With Thermal Loads of 80-60-40-20 W [273-205-137-68 BTU/h; 1m/s=3.28 ft/s]

velocity magnitude gradually decreases to a minimum above WPD that has the minimum heat load of 20 W [68 BTU/hr]. On the other hand Figure 4-14 shows that the vertical convection generated due to waste package heating has similar magnitude as all the waste packages have the same thermal loading of 75 W [266 BTU/hr]. Figures 4-13 through 4-15 also show that the relative location and magnitude of the high axial velocity region mentioned previously also depends on the thermal load distribution. The largest axial high velocity zone with maximum velocity magnitude was generated by the most uneven thermal load distribution; 80-60-40-20 W [273-205-137-68 BTU/h] as shown in Figure 4-15. The uniform distribution case with minimum heat load 50 W [170.6 BTU/hr], Figure 4-12 generated the smallest high velocity zone.

Figure 4-16 shows the temperature calculated at different cross sectional locations illustrated in Figure 4-12. The temperature distribution in the axial planes for all four 'dry' cases exhibited the same pattern of temperature distribution, though the local values were dependent on the thermal loading. A comparison of temperature contours in the YZ plane among Figures 4-16(a) through (d) shows that the temperature values were dependent on the thermal loading of the adjacent waste package. For example Figure 4-16(d) shows that the temperature above WPA which has a load of 80 W [273 BTU/hr] is higher compared to temperature above WPD, that has a load of 20 W [68BTU/hr]. This phenomenon illustrates the fact that the primary heat transfer mode in the vicinity of the waste package is two-dimensional vertical buoyancy driven convection and as illustrated previously in Figures 4-12 through 4-15, the convective velocity magnitude is dependent on the thermal loading. A qualitative comparison of temperature contours in the YZ plane between different cases also illustrates that axial velocity has only a

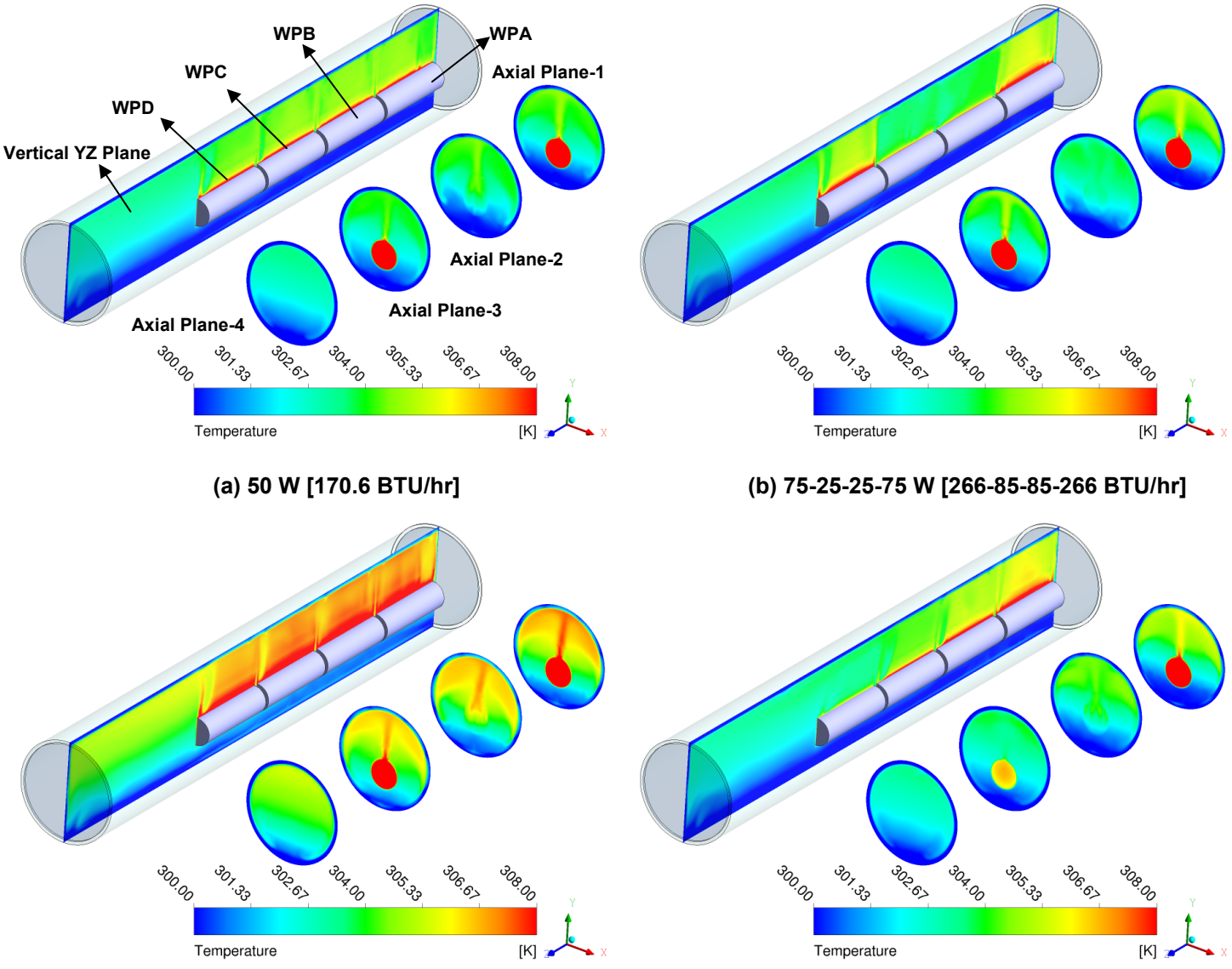

(a) 50 W [170.6 BTU/hr]

(b) 75-25-25-75 W [266-85-85-266 BTU/hr]

(c) 75 W [266 BTU/hr]

(d) 80-60-40-20 W [273-205-137-68 BTU/hr]

Figure 4-16. Temperature Contours Dry Simulations [°F = 1.8 × K–459.4]

minor impact on heat transfer from waste packages and any axial convection is likely to be small compared to vertical convection.

Waste package temperatures calculated for the 'dry' cases are illustrated in Figure 4-17. As is evident from Figure 4-17, high thermal load waste packages exhibit higher surface temperatures compared to the low thermal load waste packages. In addition, a high thermal load waste package had minimal thermal impact on an adjacent low thermal load waste package. Hence there has been little or no heat exchange between waste packages due to radiation and it can be concluded that waste package temperatures are mostly a function of the thermal load it contains.

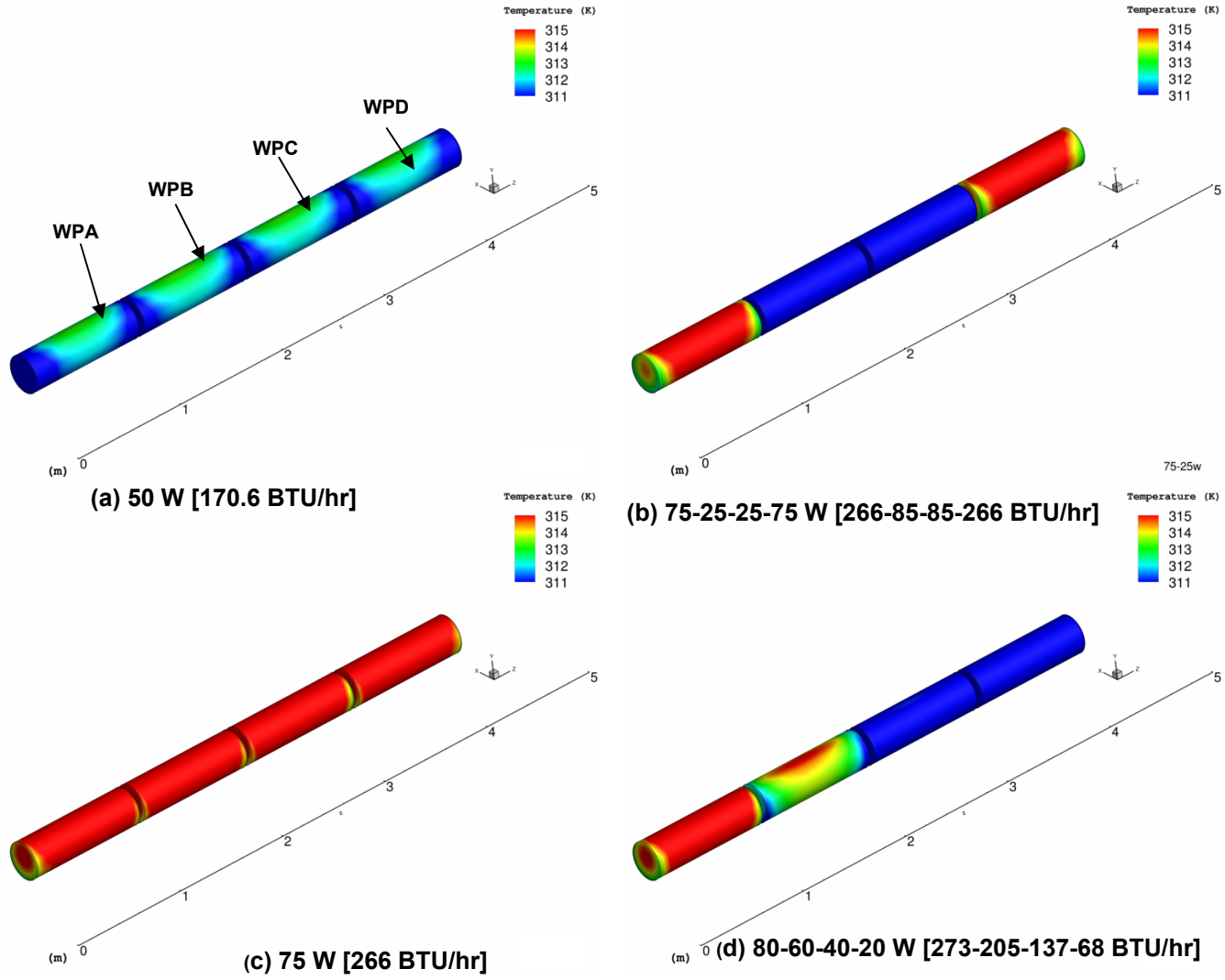

Figure 4-17. Temperature Distribution on Waste Package Surfaces [1 m =3.28 ft; °F = 1.8 × K–459.4]

Figures 4-18(a) through (d) show comparisons of experimental temperature data with computed results. These figures illustrate the section averaged temperature data as a function of the distance along the drift for all four 'dry' cases. Location of the axial cross sections are shown in Figure 4-4(a) and the section average temperature calculation procedure is explained in Figure 4-4(b). Details on the instrumentation in each section are reported in Manepally, et al. (2006) and Green (2010). The temperature results predicted here include all modes of heat transfer, including radiation, but as the domain does not have any water source, moisture transport was excluded. In general, it can be seen from Figure 4-18 that the computations were able to replicate the general trend and pattern of the experimentally observed temperature variation. Most of the temperature peaks observed in the experiment were captured in the computations. This indicates that the computations were successful in obtaining the spatial temperature variation within the domain. But it can also be observed that for all the cases, the computed results consistently overpredict the average temperature values. The difference between the computed and experimental data, however, is not constant and depends on the point of

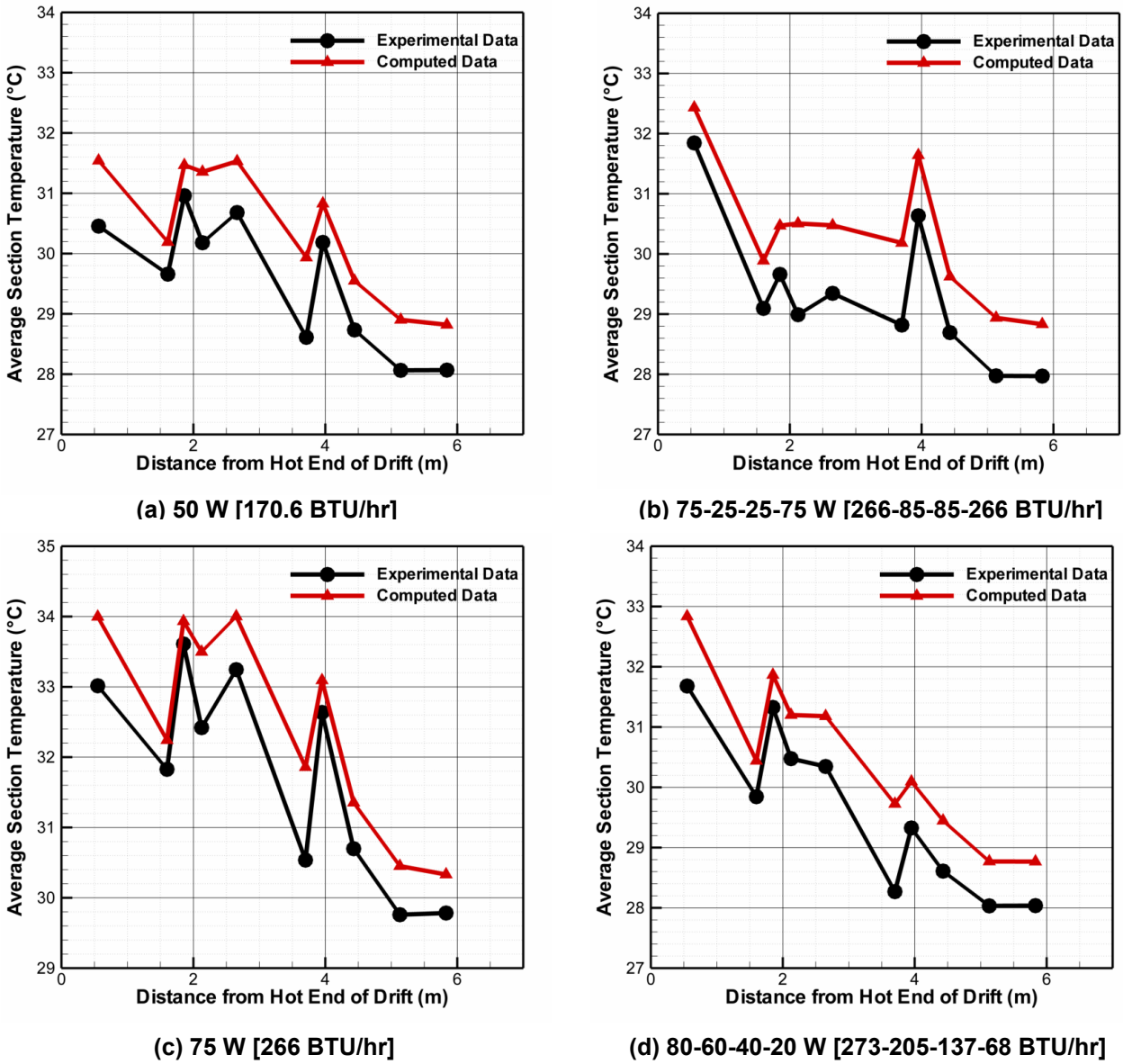

Figure 4-18. Cross Section Averaged Temperature Distribution Along the Axial Distance [1 m = 3.28 ft; °F = 1.8 × °C + 32]

observation and ranges between 2 °C [3.6 °F] to 0.3 °C [0.54 °F]. The possible reason for the discrepancy between the calculated and experimental data is discussed below in connection with Figure 4-19.

Figure 4-19 shows a comparison between computed and experimentally obtained averaged waste package temperature distributions. Contrary to what has been observed in Figure 4-18, the computed data underpredicts the average waste package temperature. The difference between computed and experimental values ranges between 2.3 °C [4.14 °F] to 0.4 °C [0.72 °F]. Results from Figures 4-18 and 4-19 show that in the computation a model excess heat is released from the waste packages and warms up the adjacent air, which causes underprediction of waste package temperatures and overprediction of section averaged air

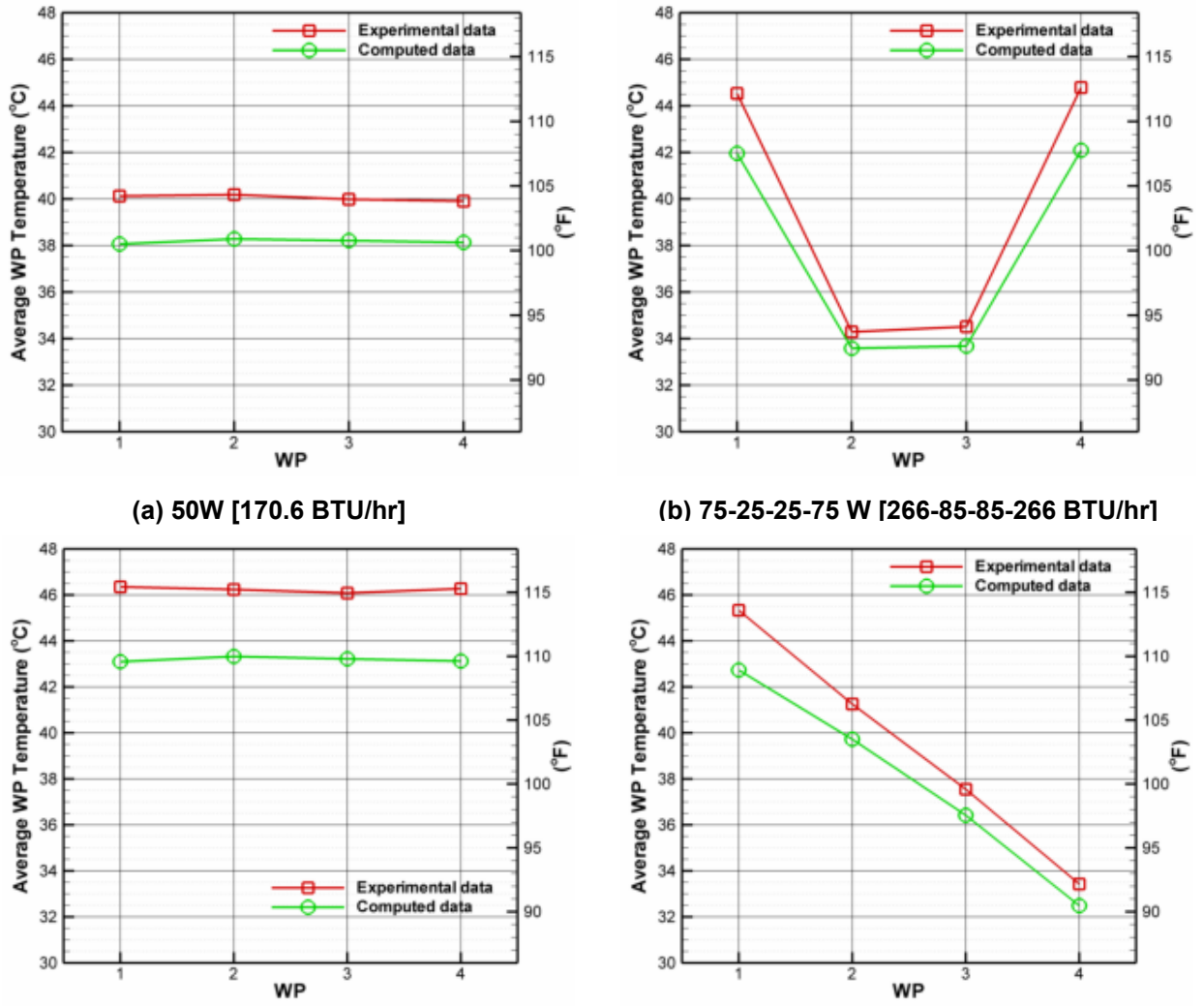

Figure 4-19. Temperature Distribution on Waste Package Surfaces [1 m = 3.28 ft; °F = 1.8 × °C + 32]

temperatures. This result can also be attributed to uncertainty in material property specification such as emissivity that controls the heat release rate from the waste packages.

To have an overall assessment of the model, temperatures obtained from the numerical solution are plotted against experimental data in Figure 4-20. It is clear that for the majority of the cases, the computed results overpredict temperature. The deviation in results, however, does not exceed 3 °C [5.4 °F].

4.2.2.2 Simulation of Moist Cases

This section discusses the computational results for the 'moist' case simulations as identified in Table 4-1. Experimental investigation for the 'moist' case was performed for one uniform thermal loading of 50 W [170.6 BTU/h] and one nonuniform loading of 75-25-25-75 W [266-85-85-266 BTU/h]. To get an understanding of the thermal effect on moisture distribution

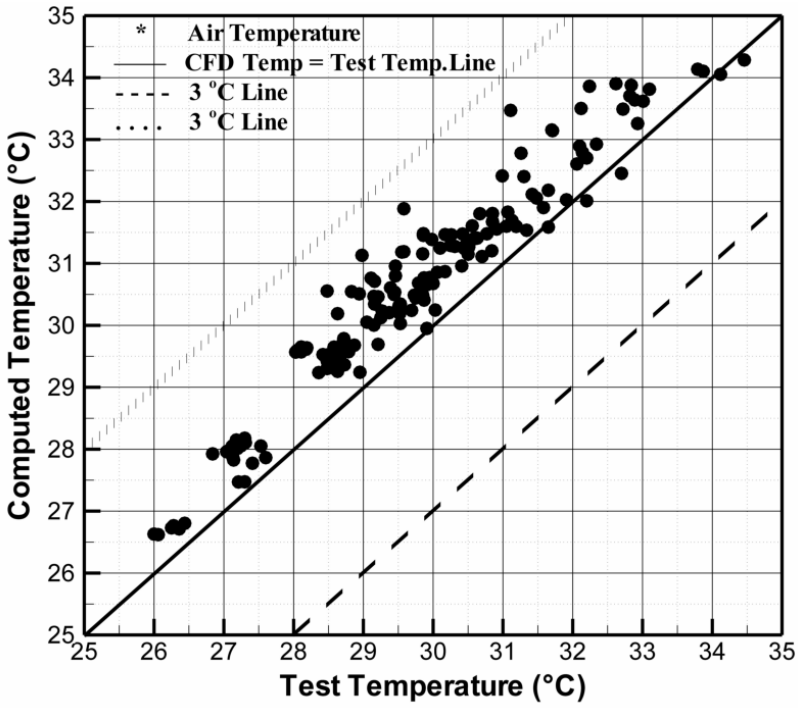

Figure 4-20. Comparison of Experimental and Computed Temperature Data for all Dry Cases With Uniform and Nonuniform Heat Load Distributions [°F = 1.8 × °C + 32]

inside the drift, the numerical study was done for all four heat loads mentioned in Table 4-1, though experimental data was available for only two cases.

The standard ANSYS-FLUENT solver along with the UDFs developed to model wall condensation-evaporation and volumetric condensation was used to obtain results for the 'moist' cases. Both equilibrium and nonequilibium models in the simulation provided very similar results for flow and temperature fields. This is because the volumetric condensation within the system was almost absent as water vapor concentration mostly remained at or below the saturation limit. The amount of water vapor generated due to evaporation of dripping water was relatively modest compared to the condensation cell chamber described in Chapter 3. Hence, results obtained from nonequilibrium model are presented and discussed in this section.

Thermocouples and humidity sensors were placed at twelve spatial locations for the 'moist' cases for both uniform and nonuniform loading. The positions of these sensors are shown in Figures 4-21 and 4-22. As shown in these figures, all probes were placed along the mid-vertical YZ plane {x=0 m [0 ft]}, and at five axial planes. Locations of these axial planes are shown in Figure 4-21. Figure 4-22 highlights the relative position of these sensors in the mid-vertical plane.

Figure 4-23 shows the axial variation of experimental and computed cross section averaged temperature for both the uniform 50 W [170.6 BTU/hr] and non uniform 75-25-25-75 W [266-85-85-266 BTU/hr] thermal loading 'moist' case. The simple sectional averaging method explained in Figure 4-4(b) is used for average temperature calculations. It can be observed in Figure 4-23 that the computational results predicted the trend of temperature variation, but have generally overpredicted the temperature. This was also observed for the 'dry' cases and

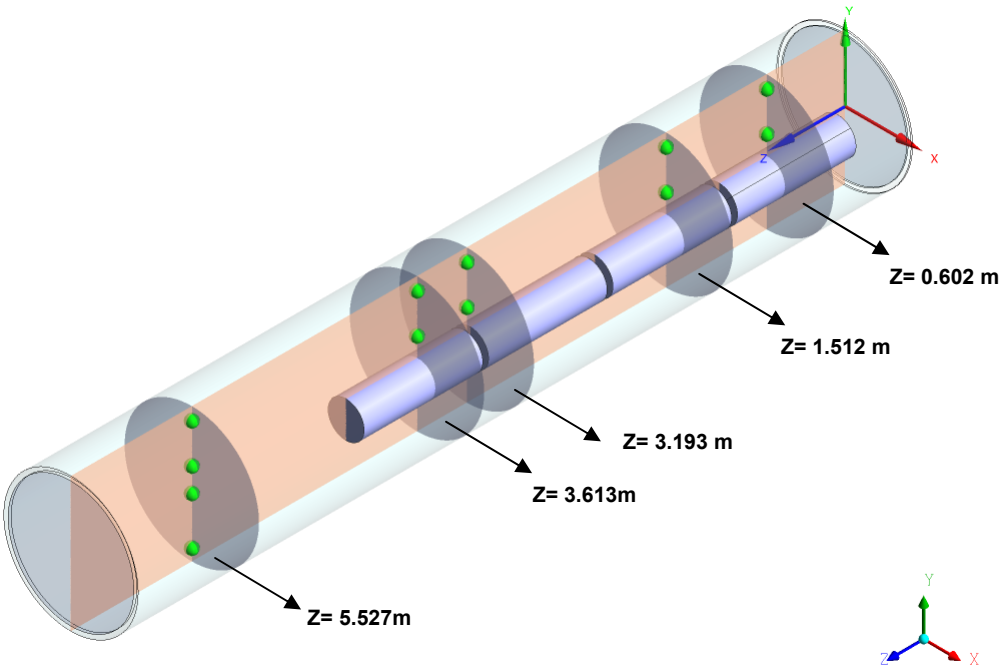

Figure 4-21. Axial Location of the Relative Humidity Probes for the Moist Case Experiments [1 m = 3.28 ft]

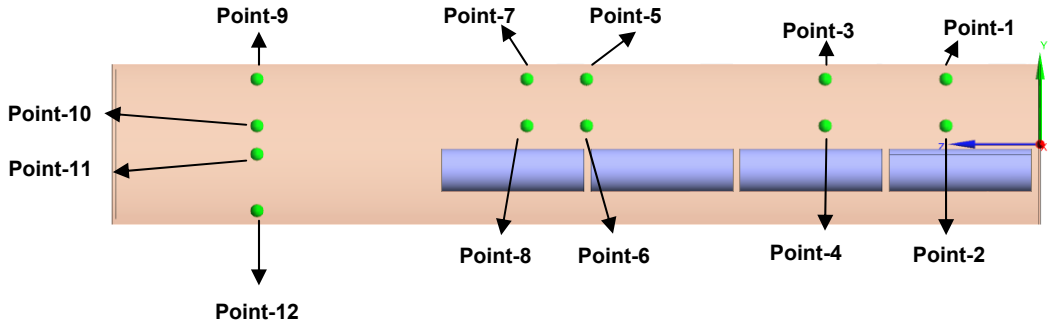

Figure 4-22. Relative Position of 12 Thermocouples and Relative Humidity Sensors in the Middle Vertical Plane

highlighted in Figure 4-18. As discussed in Section 4.2.2.1, this can be attributed to uncertainties in specifying exact material properties and other modeling parameters. It should also be noted that the experimental data was collected for a very limited number of points and does not provide a comprehensive map of the temperature variation in the axial direction. Deviation of computed data from experimental observations can also be caused by measurement uncertainties and localized unsteady flow effects.

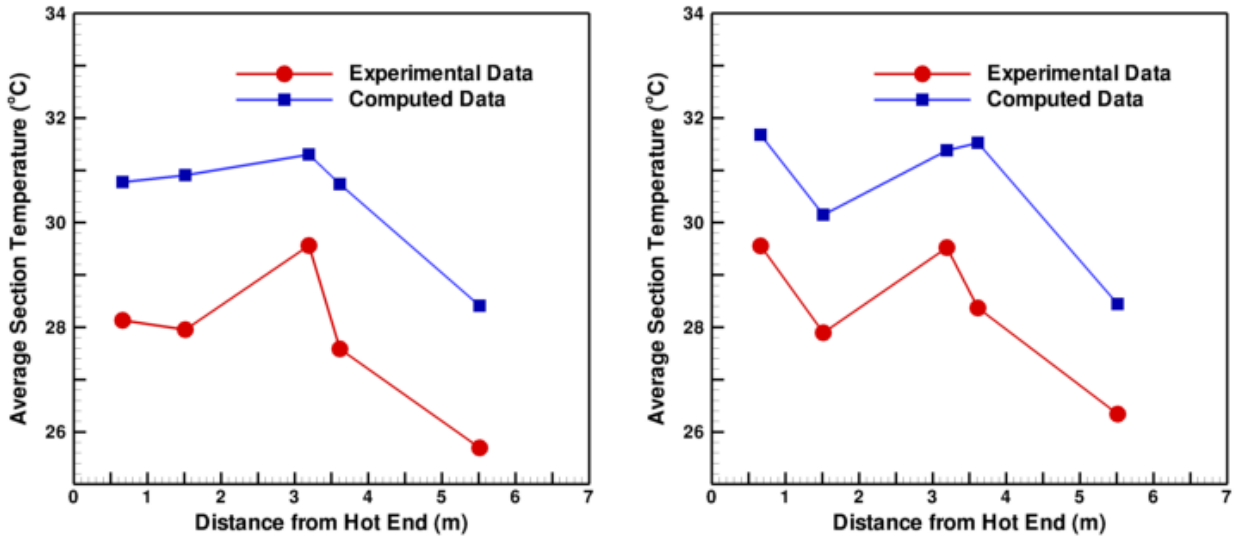

(a) 50 W [170.6 BTU/hr]

(b) 75-25-25-75 W [266-85-85-266 BTU/hr]

Figure 4-23. Cross Section Averaged Temperature Distribution Along the Axial Distance for Moist Cases [1 m = 3.28 ft; °F = 1.8 × °C + 32]

Figure 4-24 shows the overall performance of the solver in predicting air temperature at different locations within the 20-percent drift-scale with uniform and nonuniform thermal loading for 'moist' cases. It can be seen that the computations generally overpredicted temperature values, but for most of the observation points, the deviation did not exceed 3 °C [5.4 °F].

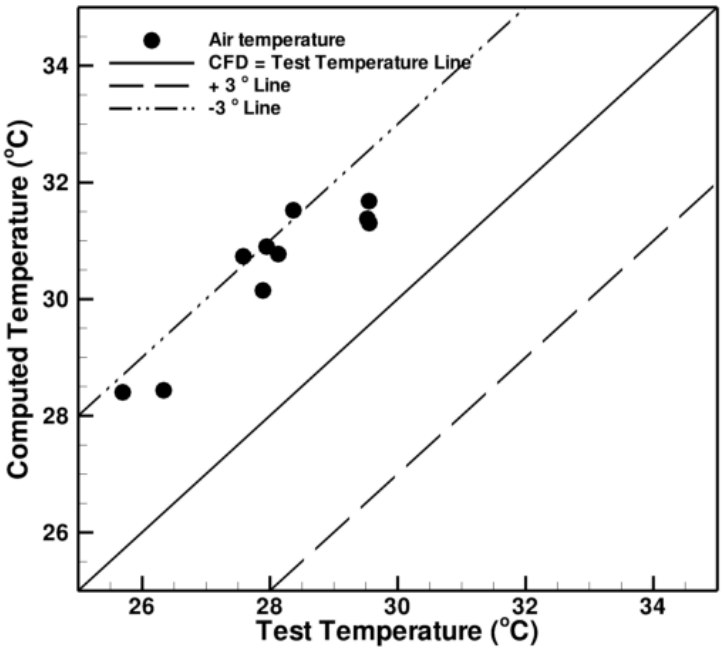

Figure 4-24. Comparison of Experimental and Computed Temperature Data for All Moist Cases With Uniform and Nonuniform Heat Load Distributions [°F = 1.8 × °C + 32]

Figure 4-25 shows the relative humidity contours for all four thermal loads. The liquid water source is on the upper half of waste package WPA. A high humidity area in the surroundings of WPA can be observed from the contours in axial-plane-1, that can be attributed to the evaporation of liquid water from the surface of WPA. The level of humidity and water vapor mass concentration, however, is dependent on the thermal load of WPA. A qualitative comparison of 4-25(a) and 4-25(d) shows that a thermal load of 50 W [170.6 BTU/hr] sustains more humidity compared to a heat load of 80 W [173 BTU/hr]. This was expected, as the air

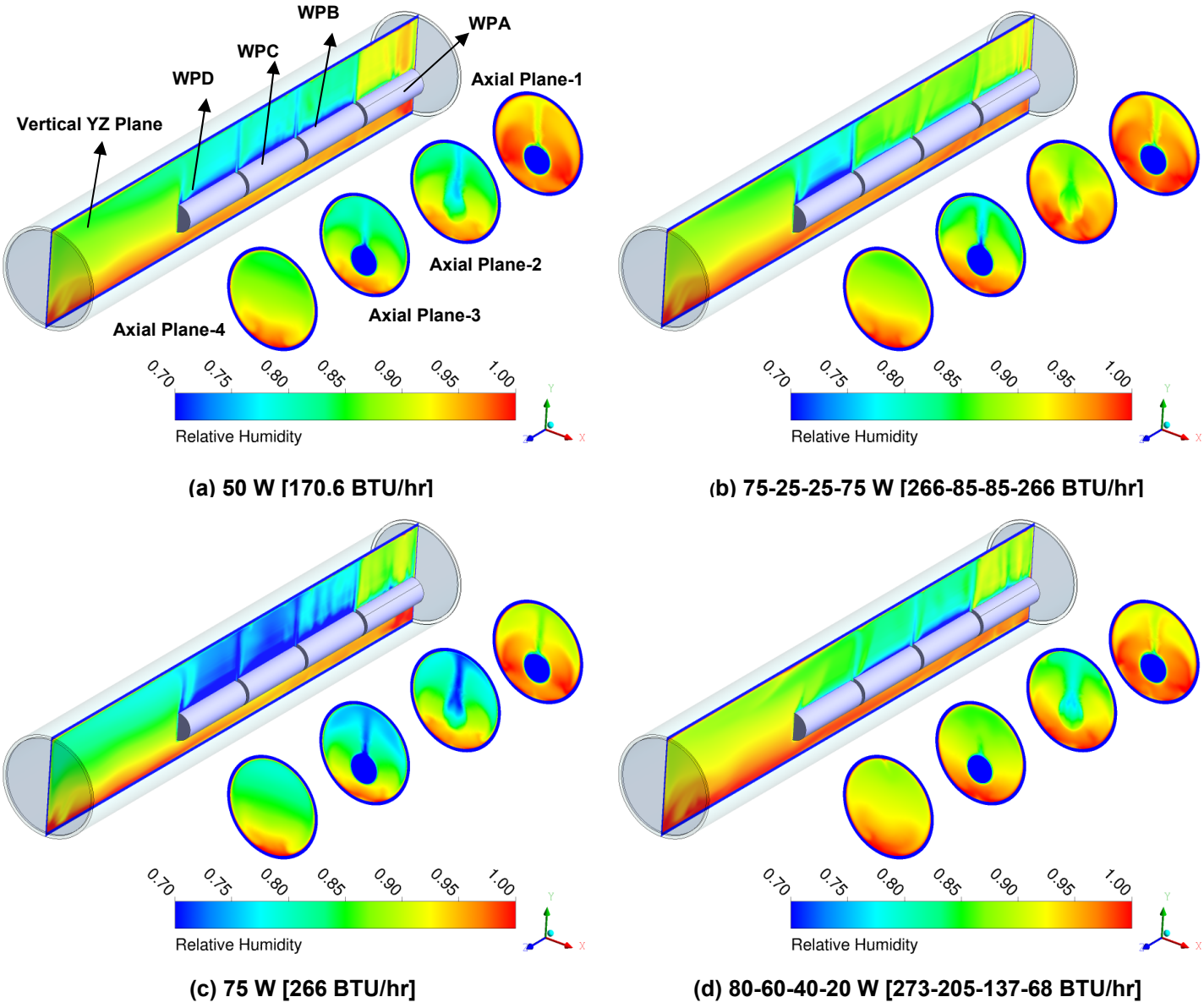

(a) 50 W [170.6 BTU/hr]

(b) 75-25-25-75 W [266-85-85-266 BTU/hr]

(c) 75 W [266 BTU/hr]

(d) 80-60-40-20 W [273-205-137-68 BTU/hr]

Figure 4-25. Relative Humidity Contours Obtained From Moist Simulations

temperature in the vicinity of a waste package is mostly controlled by the vertical convection current generated due to the waste package heat and is not significantly influenced by the axial convection or inter-waste package radiation as discussed in Section 4.2.2.1. Hence air around a high thermal load waste package has a higher temperature, as illustrated in Figure 4-16, and has a higher saturation limit that is manifested as lower relative humidity. Similar dependence of relative humidity on the waste package heat load can be observed for the rest of the waste packages as well. The relative humidity contours on axial planes show that the air below the waste package has higher relative humidity. This can also be attributed to the convection pattern of hot air as illustrated in Figures 4-12 through 4-15 that results in a low temperature zone below the waste package as highlighted in Figure 4-16. The relative humidity near the cold end of the domain is also higher due to relatively cooler temperature in that region.

Figure 4-26 compares the experimental and computed relative humidity data. The axial variation of relative humidity for the 'moist' uniform 50 W [170.6 BTU/hr] thermal loading is presented in Figure 4-26(a) and for 'moist' nonuniform 75-25-25-75 W [266-85-85-266 BTU/hr] thermal loading is presented in Figure 4-26(b). In general, the relative humidity initially decreases with axial distance from the hot end and subsequently increases with axial distance away from the waste packages. Deviation of this pattern for the 75-25-25-75 W [266-85-85-266 BTU/hr] 'moist' case at z = 1.512 m [4.96 ft] was caused by a malfunctioning relative humidity probe and should be ignored. For both uniform and nonuniform thermal loading, computed results overpredict relative humidity near the hot end and then underpredict data away from the hot end. The overprediction of relative humidity near the hot end can be associated with uncertainty in estimation of liquid water mass. The evaporation model uses surface area and surface temperature as input to calculate the steady vaporization rate. It does not take into account the effect of limited liquid water dripping that was done in the experiment

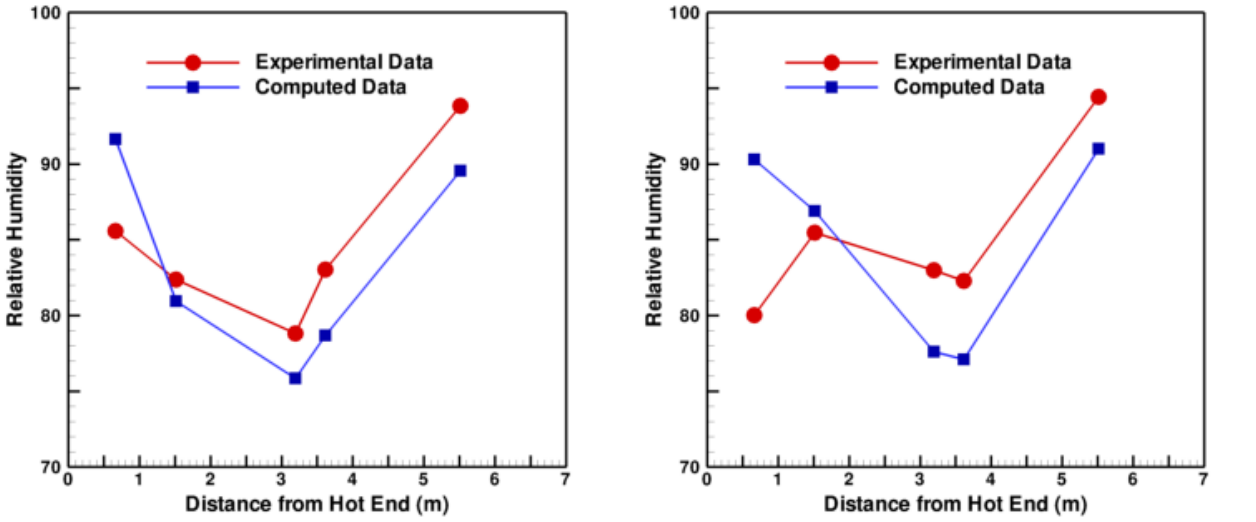

(a) 50 W [170.6 BTU/hr] **(b) 75-25-25-75 W [266-85-85-266 BTU/hr]**

Figure 4-26. Cross Section Averaged Relative Humidity Distribution Along the Axial Distance for Moist Cases [1 m = 3.28 ft]

or any unsteady effect associated with it. As a result, the computational model allows more water to vaporize and causes higher relative humidity near the hot end. Similarly, the difference in condensation rate between the experimental observation and computational estimate is responsible for the deviation in relative humidity away from the hot end.

Figure 4-27 shows the overall variation of the computed relative humidity data with the experimental data and it is shown that the calculated relative humidity values lie within 10 percent of the experimental data except at a single location. As mentioned previously, this deviation was caused by instrumentation malfunction and should be neglected.

4.3 Summary

A 20-percent scale model of the proposed emplacement drift at Yucca Mountain was developed to study the heat and moisture transportation due to radioactive decay heat and liquid water. The experiment was also conducted to benchmark and test the customized UDFs developed for modeling the condensation and evaporation processes to be used in conjunction with the baseline ANSYS-FLUENT CFD solver.

Two sets of tests were performed to understand the waste package heat driven natural convection and moisture transport separately. In the first set of tests, no moisture was allowed inside the domain and tests were conducted for two uniform and two nonuniform thermal loading scenarios. In the second set of tests, liquid water was dripped on the first waste package which evaporated to form moist air within the system. One uniform and one nonuniform thermal loading was considered for the 'moist' system.

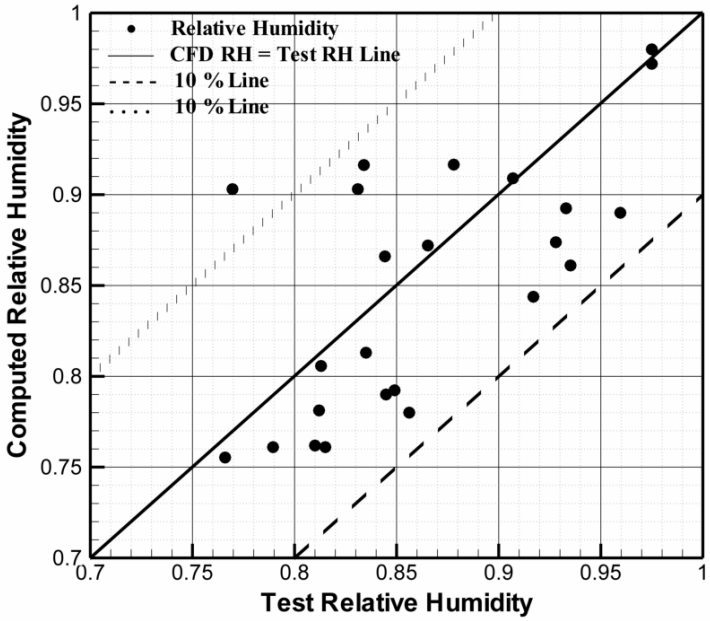

Figure 4-27. Comparison of Experimental and Computed Relative Humidity for the Moist Cases With Uniform 50 W [170.6 BTU/hr] and Nonuniform 75-25-25-75 W [266-85-85-266 BTU/hr] Thermal Load Distributions

A three dimensional model was developed using ANSYS-FLUENT for the 20-percent scaled model. For the ‘dry’ cases, the baseline solver was used to model conduction, natural convection and thermal radiation heat transfer. The discrete ordinate radiation model was used for radiation modeling. For the ‘moist’ cases, wall condensation and evaporation was simulated using the customized UDFs. As some initial simulations exhibited negligible volumetric condensation, only the nonequilibium model was used for the ‘moist’ case simulations.

The flow field obtained from the ‘dry’ cases showed a strong two-dimensional convection cell in the axial plane around a waste package, where a hot air plume moved vertically upwards. The velocity magnitude of air in these localized cells was directly dependent on the waste package thermal load and was not significantly dependent on the heat load of neighboring waste packages. Away from the heated waste packages, the two dimensional axial convection current was dominant. The flow below the waste packages is not representative of that of the 20-percent drift-scale model because the metallic stands of the waste packages were not included in the CFD model. In the absence of the stands, the flow below the waste packages is mainly axial, moving from the cold end to the hot end. A comparison of experimental and computed data showed that ANSYS-FLUENT generally overpredicted the temperatures, but the deviation did not exceed 3 °C [5.4 °F]

The ‘moist’ case simulations showed that the relative humidity and the water vapor concentration around the waste package were mostly dependent on the heat load of the waste package and showed minimal effect of axial convection current or the heat load of neighboring waste packages. The computed solution overpredicted relative humidity near the water source at the hot end and underpredicted relative humidity away from the waste packages near the cold end. The temperature values obtained from the simulations were consistently higher compared to the experimental data, but the maximum difference was in the range of 3 °C [5.4 °F].

5 SUMMARY

The in-drift repository environment is a result of a complex interactions among a number of thermal, hydrological and chemical processes. The heat transfer mechanism inside the drift involves conduction, natural convection, and radiation as well as latent heat transfer. Liquid water inside the drift evaporates from hotter surfaces, convects to a relatively cooler location and condenses to form liquid water. This redistribution of water can affect the long-term integrity of the engineered barrier system.

General computational fluid dynamics (CFD) tools have been extensively used to simulate flow and thermal fields for a variety of applications. The broad objective of the study was to develop a general CFD modeling framework that is useful for simulating the flow, heat and mass transfer within an emplacement drift. The modeling exercise was supported by experimental studies that provided valuable data for validation and benchmarking.

A general purpose CFD tool ANSYS-FLUENT® has been adapted for simulation of in-drift flow, heat and mass transfer processes. The standard solver was used to simulate the natural convection and multimode heat transfer processes including radiation. The solver was also capable of tracking water vapor movement within the domain by solving the species transport equations. Customized tools for modeling surface condensation, volumetric condensation and surface evaporation were developed and linked with the solver as User Defined Functions (UDFs). Two different approaches to model volumetric condensation using equilibrium and nonequilibium models were developed and tested. Data from supporting experimental studies were used for verification and benchmarking of computed data.

Two different sets of combined experimental and computational investigations were described in this report. The first study was conducted in a closely controlled environment, where a condensation-evaporation cycle was created within an enclosure using a water source and cold plate at constant temperatures. The experimental study was conducted for a range of temperature differences between the cold plate and hot water source. Subsequently, a numerical study was conducted to simulate the experimental setup. The results showed the velocity, temperature, and relative humidity distribution of the system. It was observed that the equilibrium model provided a better match with the experimental condensation rate and temperatures.

The second experimental and computational study was conducted using a 20-percent scale model of the proposed emplacement drift at Yucca Mountain. Two different sets of experiments were conducted. In the first set, no liquid water was introduced into the system and the experiment was conducted for a uniform and nonuniform thermal loading of waste packages. Temperature measurements were taken for a number of spatial locations within the experimental setup. A numerical model was developed to simulate the experimental setup with no moisture using ANSYS-FLUENT. Computed velocity patterns showed existence of strong two-dimensional convection cells in the vicinity of the waste packages, where the air moves vertically upwards. This motion was found to be controlled by the waste package heat load and was almost independent of the axial convection or the thermal loading of any neighboring waste packages. A comparison of experimental and computed data showed that ANSYS-FLUENT generally overpredicted the temperatures, but the deviation did not exceed 3 °C [5.4 °F]. The second set of experimental and computational studies included the effect of liquid water. A source of liquid water on the upper surface was established. The liquid water subsequently evaporated and was transported to a cooler location by natural convection. The experimental

study measured the relative humidity and temperature data. Simulation results showed that like velocity, relative humidity and water vapor concentration around the waste package was mostly dependent on the heat load of the waste package. The computed solution overpredicted relative humidity data near the water source at the hot end and underpredicted relative humidity away from the waste packages near the cold end. The computed results overpredicted temperature values, but the deviation did not exceed 3 °C [5.4 °F].

From the comparison of experimental and numerical results from the above mentioned studies, it can be concluded that the ANSYS-FLUENT baseline solver was able to predict the general trend and pattern of the convective airflow and heat transfer. The deviation in temperature predicted between the computed and experimental data was bounded within a small range. The relative humidity and condensation rate results obtained from the combined baseline solver along with the UDFs provided results comparable to the experiments, but there was some deviation of predicted values from experimental data. Overall results indicate the modeling framework and supplementary customized UDFs developed using ANSYS-FLUENT can be useful in investigating the in-drift repository environment to assess the flow and thermal parameters.

6 REFERENCES

ANSYS, Inc. "FLUENT® User's Guide." Version 12.1. Canonsburg, Pennsylvania: ANSYS, Inc. 2009a.

———. "ANSYS–WORKBENCH User's Guide." Version 12.1. Canonsburg, Pennsylvania: ANSYS, Inc. 2009b.

———. "ANSYS–DESIGN MODELERS User's Guide." Version 12.1. Canonsburg, Pennsylvania: ANSYS, Inc. 2009c.

———. "ANSYS–MESHING User's Guide." Version 12.1. Canonsburg, Pennsylvania: ANSYS, Inc. 2009d.

———. "ANSYS–CFD–POST User's Guide." Version 12.1. Canonsburg, Pennsylvania: ANSYS, Inc. 2009e.

———. "FLUENT® Theory Guide." Version 12.1. Canonsburg, Pennsylvania: ANSYS, Inc. 2009f.

———. "FLUENT® User Defined Functions Guide." Version 12.1. Canonsburg, Pennsylvania: ANSYS, Inc. 2009g.

Bechtel SAIC Company, LLC. "In-Drift Natural Convection and Condensation." MDL–EBS–MD–000001. Rev. 00. Las Vegas, Nevada: Bechtel SAIC Company, LLC. 2004.

Bell, B. "Application Brief: Film Condensation of Water Vapor." Lebanon, New Hampshire: Fluent, Inc. 2003.

Bird, R.B., W.E. Stewart, and E.N. Lightfoot. *Transport Phenomena*. New York City, New York: John Wiley & Sons. 1960.

Birkholzer, J.T. and G.L. Danko. "Technical Work Plan for: Thermal-Hydrological Near-Field Model Studies and Impact of Natural Convection on Seepage." OSTI–LBNL–TWP–000006. Rev. 00. Las Vegas, Nevada: DOE, Office of Civilian Radioactive Waste Management, Office of Science and Technology and International. 2005.

Brouwers, H.J.H. and A.K. Chester. "Film Models for Transport Phenomena With Fog Formation: The Classical Film Model." *International Journal of Heat and Mass Transfer.* Vol. 35. pp. 1–11. 1992a.

———. "Film Models for Transport Phenomena With Fog Formation: The Fog Film Model." *International Journal of Heat and Mass Transfer.* Vol. 35. pp. 13–28. 1992b.

Buscheck, T.A., L.G. Glascoe, and K.H. Lee. "Validation of the Multiscale Thermohydrologic Model Used for Analysis of a Proposed Repository at Yucca Mountain." *Journal of Containment Hydrology*. pp. 62–633. 2003.

Carey, V.P. *Liquid-Vapor Phase-Change Phenomena*. 2nd Edition. New York City, New York: Hemisphere Publishing Corporation. 2007.

Das, K. and D. Basu. "Validation of Computational Fluid Dynamics Modeling Approach to Evaluate VSC-17 Dry Storage Cask Thermal Designs." San Antonio, Texas: CNWRA. 2007.

Das, K., D. Basu, and K. Axler. "Validation of Modeling Approach To Evaluate Transportation, Aging, and Disposal Canister Thermal Designs." San Antonio, Texas: CNWRA. 2008.

Danko, G. and D. Bahrami. "Barometric Pressure Variation Effects on Emplacement Drift Environmental Conditions at Yucca Mountain." Proceedings of the 11th International High-Level Radioactive Waste Management Meeting, Las Vegas, Nevada, April 30–May 4, 2006. La Grange Park, Illinois: American Nuclear Society. pp. 353–360. 2006.

———. "Heat and Moisture Flow Simulation with Multiflux." ASME Heat Transfer/Fluids Summer Conference, Charlotte, North Carolina. New York City, New York: ASME International. 2004.

———. "Powered, and Natural, Passive Ventilation at Yucca Mountain." Proceedings of the 8th International High-Level Radioactive Waste Management Meeting, Las Vegas, Nevada, March 30–April 2, 2003. La Grange Park, Illinois: American Nuclear Society. pp. 683–690. 2003.

Fedors, R.W., S. Green, D. Walter, G. Adams, D. Farrell, and S. Svedeman. "Temperature and Relative Humidity Along Heated Drifts With and Without Drift Degradation." CNWRA 2004-04. San Antonio, Texas: CNWRA. 2004.

Fedors, R.W., D.B. Walter, F.T. Dodge, S.T. Green, J.D. Prikryl, and S.J. Svedeman. "Laboratory and Numerical Modeling of the Cold-Trap Process." San Antonio, Texas: CNWRA. 2003a.

Fedors, R.W., G.R. Adams, C. Manepally, and S.T. Green. "Thermal Conductivity, Edge Cooling, and Drift Degradation—Abstracted Model Sensitivity Analyses for Yucca Mountain." San Antonio, Texas: CNWRA. 2003b.

Flow Science, Inc. "FLOW-3D® User's Manual." Version 9.0. Santa Fe, New Mexico: Flow Science, Inc. 2005.

Fox, R.J., P.F. Pederson, M.M.L. Corradini, and A.P. Pernsteiner. "Free Convective Condensation in a Vertical Enclosure." *Nuclear Engineering and Design*. Vol. 177, Nos. 1–3. pp. 71–89. 1997.

Green, S. "Cold Trap CFD Modeling." Scientific Notebook Number 536E. San Antonio, Texas: CNWRA. 2010.

Green, S. and C. Manepally. "Software Validation Test Plan for FLOW-3D Version 9." Rev. 1. San Antonio, Texas: CNWRA. 2006.

Green, S.T., D.B. Walter, R.W. Fedors, and F.T. Dodge. "A Model for Moisture Transport in a High-level Radioactive Waste Repository Drift." Proceedings of the Society for Mining, Metallurgy, and Exploration Annual Meeting, February 23–25, 2004. Denver, Colorado: Society for Mining, Metallurgy, and Exploration. Published on CD ROM. 2004.

Hijikata K. and Y. Mori. "Forced Convective Heat Transfer of a Gas With Condensing Vapor Around a Flat Plate." *Heat Transfer Japanese Research.* Vol. 2. pp. 81–101. 1973.

Incropera, F.P. and D.P. Dewitt. *Fundamentals of Heat and Mass Transfer*. 4th Edition. New York City, New York: John Wiley & Sons, Inc. 1996.

Kang, H.C. and M.H. Kim. "Characteristics of Film Condensation of Supersaturated Steam–Air Mixture on a Flat Plate." *International Journal of Multiphase Flow.* Vol. 25, No. 8. pp. 1,601–1,618. 1999.

Kuehn, T.H. and R.J. Goldstein. "An Experimental Study of Natural Convection Heat Transfer in Concentric and Eccentric Horizontal Cylindrical Annuli." *ASME Journal of Heat Transfer*. Vol. 100. pp. 635–640. 1978.

———. "An Experimental Study and Theoretical Study of Natural Convection in the Annulus Between Horizontal Concentric Cylinders." *Journal of Fluid Mechanics*. Vol. 74, Part 4. pp. 695–719. 1976.

Manepally, C., S. Green., F. Viana, and R. Fedors. "Evaluation of In-Drift Heat Transfer Processes." San Antonio, Texas: CNWRA. 2006.

Menter, F.R. "Two-Equation Eddy-Viscosity Turbulence Models for Engineering Applications." *American Institute of Aeronautics and Astronautics Journal*. Vol. 32, No. 8. pp. 1,598–1,605. 1994.

Popiel, C.O. and J. Wojtkowiak. "Simple Formulas for Thermophysical Properties of Liquid Water for Heat Transfer Calculations (0oC to 150oC)." *Heat Transfer Engineering.* Vol. 19, No. 3. pp. 87–101. 1998.

Reynolds, W.C. "Thermodynamic Properties in SI: Graphs, Tables, and Computational Equations for Forty Substances." Palo Alto, California: Stanford University, Department of Mechanical Engineering. 1979.

Rhie C.M. and W.L. Chow. "Numerical Study of the Turbulent Flow Past an Airfoil With Trailing Edge Separation." *American Institute of Aeronautics and Astronautics Journal*. Vol. 21. pp. 1,523–1,532. 1983.

Salari, K. "Adaptive Coupling Techniques for CFD and Porous Flow." Engineering Research and Technology Report. Livermore, California: Lawrence Livermore National Laboratory. 2005

Sparrow, E.M., W.J. Minkowycz, and M. Saddy. "Forced Convection Condensation in the Presence of Noncondensables and Interfacial Resistance." *International Journal—Heat Mass Transfer*. Vol. 10. pp. 1,829–1,845. 1967.

Van Doormal, J.P. and G.D. Raithby. "Enhancements of the SIMPLE Method for Predicting Incompressible Fluid Flows." *Numerical Heat Transfer.* Vol. 7. pp. 147–163. 1984.